

MASTER THESIS

**Stratocumulus Cloud Response to
changing large-scale forcing
conditions**

Author:
Jasper Sival

Supervisors:
Dr. Stephan de Roode
Ir. Jerome Schalkwijk

CLOUDS, CLIMATE AND AIR QUALITY
DEPARTMENT OF MULTI-SCALE PHYSICS
FACULTY OF APPLIED SCIENCES

DEPARTMENT OF GEOSCIENCE AND REMOTE SENSING
FACULTY OF CIVIL ENGINEERING AND GEOSCIENCE

DELFT UNIVERSITY OF TECHNOLOGY

October 1, 2012

Abstract

The influence of the stratocumulus cloud feedback on a changing climate is not well understood. To gain more understanding of the influence, GPU Accelerated Large Eddy Simulations (GALES) are used to investigate steady-state solutions in the current climate and in a warmer climate. A warmer climate has been simulated by a sea surface temperature (SST) increase of 2 K. Given a SST increase of 2 K, a constant Low Tropospheric Stability (LTS) and a free atmospheric specific humidity which increases in addition to an increase of surface specific humidity, it has been found that stratocumulus clouds become thinner which means that they provide a positive feedback in a warmer climate.

To obtain steady-state solutions, it is necessary to use a constant solar radiative forcing. The effect of using either a constant or a diurnally varying shortwave radiative forcing on the cloud layer depth has been assessed from simulations of the EUROCS stratocumulus case. It is found that the stratocumulus' diurnally mean cloud thickness is slightly less when a constant diurnally averaged radiative forcing is used, as compared to a full diurnal cycle.

A mixed-layer model analysis shows that three distinct regions are possible in a phase space defined by the LTS and free atmospheric specific humidity. These are a stratocumulus topped boundary layer, clear convective boundary layer, and stable clear boundary layer. Also the effect of small changes of some key atmospheric variables, including the sea surface temperature (SST), large-scale divergence and wind speed has been investigated. Considering a *SST* increase, if the specific humidity of the free atmosphere does not change in a perturbed climate, there will be a positive feedback. If however the specific humidity of the free atmosphere changes as much as the surface specific humidity, a negative feedback has been found.

Contents

1	Introduction	4
1.1	Stratocumulus	5
1.2	Dynamics	7
1.3	Research goal	8
1.3.1	GALES and the Mixed-Layer Model	9
1.4	Outline	9
2	Theory	10
2.1	Thermodynamics	10
2.1.1	Moisture variables	12
2.1.2	The virtual (potential) temperature	13
2.2	Governing equations	15
2.2.1	Conservation of mass	15
2.2.2	Conservation of momentum	16
2.2.3	Conservation of heat/total water	16
2.3	Turbulent Kinetic Energy (TKE)	17
3	Modelling the STBL	18
3.1	Large Eddy Simulation (LES)	18
3.1.1	The LES filtered equations	19
3.1.2	Subfilter-scale model	20
3.1.3	Model of the incoming solar radiation	21
3.2	The Mixed-Layer Model	23
3.2.1	Entrainment in a clear boundary layer	27
3.2.2	Entrainment in a STBL	28
3.2.3	Cloud-top entrainment instability (CTEI)	28
3.2.4	Steady-state	30
3.2.5	Determining the cloud base height in the MLM	33
4	EUROCS: GALEs results of the stratocumulus case	35
4.1	Setup	35
4.1.1	Initial and boundary conditions	35
4.1.2	Large scale forcings	36

4.2	Results	37
4.2.1	Case 1: $SST = 289$ K, diurnal radiation cycle	37
4.2.2	Case 2: $SST = 289$ K, constant diurnally averaged radiation	40
4.2.3	Comparison between case 1 and 2	40
5	CGILS: using GALES to obtain steady-state solutions of the STBL	45
5.1	Case setup	45
5.1.1	GALES	48
5.2	Results	48
5.2.1	Control case	48
5.2.2	Control set	51
5.2.3	P2K set	57
5.2.4	Comparison with the Single Column Model Ec-Earth	58
5.2.5	Thermodynamic stability analysis	59
6	Mixed-Layer Model: equilibrium states of an initially clear/cloudy ABL	63
6.1	Case setup	63
6.1.1	Steady-state analytic solutions for an initially clear ABL	64
6.1.2	Case: cloudy ABL	65
6.2	Numerical solutions	66
6.2.1	Experiment 1	66
6.2.2	Experiment 2	69
6.2.3	Experiment 3	71
7	A sensitivity study of Liquid Water Path for the STBL	74
7.1	Case setup	74
7.2	Numerical results	76
8	Conclusions and recommendations	79
8.1	Conclusions	79
8.1.1	CGILS: GALES steady-state analysis	79
8.1.2	EUROCS	79
8.1.3	Equilibrium states with the Mixed-Layer Model	80
8.1.4	Sensitivity analysis of LWP with the Mixed-Layer Model	80
8.2	Recommendations	81
8.2.1	A diurnal cycle of the solar radiation	81
8.2.2	CGILS	81
8.2.3	Mixed-Layer Model sensitivity study	81
	Bibliography	1

A Namoptions GALES for the EUROCS case	3
B CGILS: namoptions GALES for the control case	7

Chapter 1

Introduction

Weather plays an important role in everyone's daily life. Many daily activities depend on whether it is cloudy and rainy or if it is a hot and dry day. Therefore it is important to know what weather one can expect. Weather forecasts are done with numerical weather models. The weather forecasts are however not always accurate. Therefore, a lot of work is being done to validate and improve those models.

Climate is defined as the mean weather (including precipitation, temperature, sunshine) over the large period of 30 years. A theme of growing importance is global climate change. The scientific consensus is that due to human activities (emissions of carbon dioxide, methane) the global temperature is likely to increase (IPCC, 2007). So far however it is uncertain what the effect is on clouds. Clouds reflect much of the incoming solar radiation back to space which leads to lower surface temperatures. On the other hand clouds also enhance the longwave radiation emitted to the surface of the Earth. In general clouds have a cooling effect in areas of low latitude because the reflected solar radiation is much higher than the trapped longwave radiation. In regions of high latitude it is the opposite; over the course of a year the net reflected solar radiation is smaller than the trapped longwave radiation, resulting in higher temperatures (Curry and Ebert, 1992).

In a changing climate more water will evaporate which could lead to more cloud formation. But in a warmer climate the atmosphere can also contain more water vapour which could lead to less clouds. It seems that there is a subtle competition between the different atmospheric reactions. Clouds could also transition into other types of clouds which all possess their own characteristics and contribution to a changing climate. The contribution of each of these types of clouds is also differently predicted by the models.

The combined response of all these effects provides a large uncertainty in the role clouds play in a changing climate as Figure 1.1 shows.

For those 12 climate models there is an even contribution of increased Planck radiation (increased longwave absorption due to the greenhouse effect

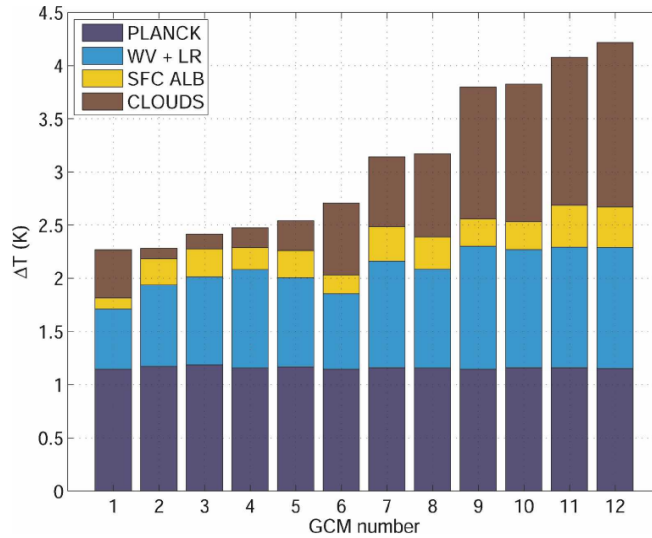


Figure 1.1: Change of the temperature ΔT for 12 different climate models due to a sudden doubling of the CO_2 concentration. There are four different effects: increased longwave radiation absorption due to Planck's law, increased longwave radiation absorption due to water vapor + lapse rate, a lower surface albedo and a highly uncertain cloud contribution. (Dufresne and Bony, 2008)

of CO_2). The second and third effect is more longwave radiation absorption due to more water vapor in the atmosphere and melting of the polar ice caps which can be accounted for a lower surface albedo. The combined contribution of these three effects is predicted roughly equally by the 12 models. The last contribution however is the effect of clouds and Figure 1.1 shows that there is a significant difference between the models. To reduce the uncertainty it is therefore very interesting to improve the understanding of the cloud influence on a warmer climate.

1.1 Stratocumulus

This thesis focuses on one type of cloud: stratocumulus. Stratocumulus (henceforth Sc) are low level clouds located at about 1 km height and are usually a few hundred meters thick. This type of cloud, together with cumulus and stratus, are the most abundant in the atmosphere. They consist of a very large number of small water droplets which have the property that they scatter a large part of the radiation. Combined with the fact that they cover a big area (sometimes in the order of 10^6 km^2) they reflect much of the incoming solar radiation. In order to maintain Sc clouds, sufficient vertical transport of moisture is needed. This is why Sc are mostly found across the

sea or ocean surface. Another prerequisite of the existence of Sc clouds is a relatively cool atmosphere. That is why Sc are mostly found across cool ocean currents. These are in the subtropical areas west of the American continent and Africa as Figure 1.2 shows.

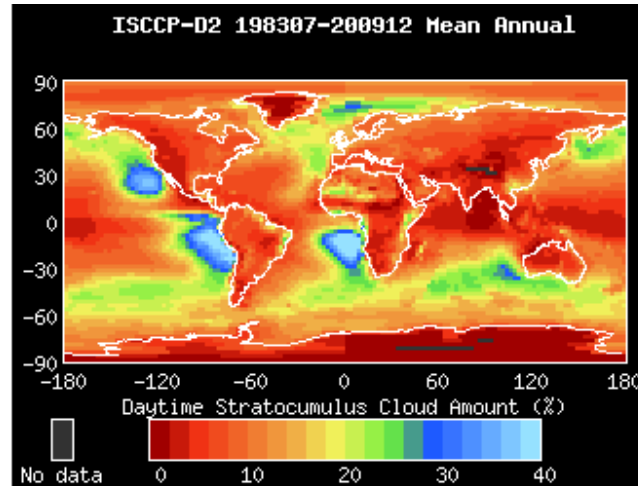


Figure 1.2: The daytime annual mean global stratocumulus amount for the period 1983-2009 (ISCCP).

Sc clouds are also supported by the downward vertical velocity of air typically present in the vicinity of high pressure systems. This flow pattern in the subtropics can be characterized by the so-called Hadley circulation which is being illustrated by Figure 1.3.

In the tropics rising air caused by the strong evaporation of water reaches the free atmosphere, which is the air above the Atmospheric Boundary Layer (ABL), and is being advected to the subtropics at 30° latitude where it descends. This descending air has generally a much higher temperature than the ABL which causes a very stable stratification. This stratification encourages the formation of Sc clouds. The intersection between the ABL with cool air and the free atmosphere with warm air defines the inversion.

Sc clouds are advected back by the trade winds from the subtropics to the tropics, which goes along with a sea surface temperature (SST) increase. This *SST* increase, together with a decreasing subsidence causes the inversion to gradually grow where Sc transition to shallow cumulus and subsequently cumulus clouds (Cu). Cu clouds have a much smaller area coverage than Sc clouds. In this transition from Sc to Cu the consequence is that more solar radiation reaches the sea surface.

One of the things that might happen in a changing climate associated with a *SST* increase is that Sc tend to transition to Cu clouds which would give a positive feedback on the temperature.

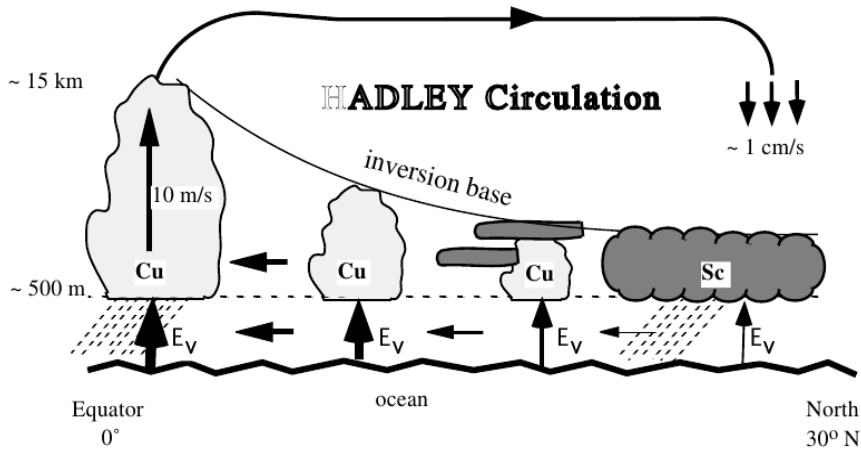


Figure 1.3: A schematic illustration of the Hadley circulation. At the tropics rising air due to a strong evaporation reaches the free atmosphere and is being advected to the subtropics where it descends and a strong inversion is formed. This stratification encourages the formation of Sc clouds which will then be advected back across the oceans to the tropics in which a transition to Cu takes place.

1.2 Dynamics

If we consider an ascending moist air parcel, the temperature decreases with height. At a certain height, the temperature of the air parcel gets sufficiently low to become saturated. The water vapour in the air parcel condenses to liquid water together with a release of latent heat and clouds are formed. Sc clouds are maintained by the vertical transport of moisture which is caused by turbulent eddies. This turbulence is mainly produced by the longwave radiative cooling at the cloud top. Because Sc clouds are optically thick they act as blackbody radiators. At the cloud top there is a net loss of longwave radiation because the cloud emits more than it absorbs from above. Due to this net radiative cooling air parcels at the cloud top can obtain a higher density such that they will sink. In addition to rising motions due to condensation these processes maintain the turbulence in the cloud layer.

Another important effect is that if turbulent eddies are strong enough they can overshoot into the free atmosphere, which is the air above the inversion. As they are colder than the free atmosphere air, they will sink and drag some of the free atmosphere air with them. This mixing of free atmosphere air with cloudy air is called entrainment. This entrainment mechanism causes a drying and a warming tendency of the ABL which can result in the thinning and eventually breakup of Sc clouds. This entrainment is dependent on many parameters like the surface fluxes of heat and

moisture, the cloud layer depth and longwave radiative cooling which makes it a very complex process. In any case entrainment tends to a rise of the inversion.

1.3 Research goal

This research focuses on two questions:

1. What is the effect of large-scale conditions (ie. $x \in \{\text{Divergence, SST, LTS, } q_{FA}, \text{ wind speed}\}$) on the equilibrium cloud depth?
2. How big is the change in cloud depth for a change in x ?

To achieve this goal we use an idealized setting to study equilibrium states according to CFMIP-GCSS Intercomparison of Large-Eddy and Single-Column Models (CGILS) (Zhang and Bretherton, 2008). CGILS has been set up to quantify the feedback mechanism of clouds in a perturbed climate. By using idealized large-scale conditions, (ie. constant SST, constant free atmosphere, constant LTS) it is possible to obtain equilibrium states of the cloud depth of Sc. This cloud depth, which is closely related to the Liquid Water Path (LWP) determines the albedo of the cloud and thus has a direct effect on the radiation balance of the Earth.

There are three parameters which control the thickness of the cloud: the specific humidity, the temperature and the pressure (q, T, p). These parameters determine the cloud base height where the air becomes saturated and water vapour condenses into liquid water, and the inversion height which is approximately the cloud top. It is therefore interesting to find solutions of these three parameters.

Entrainment is an important variable for this because on the one hand it causes the inversion to grow, causing the ABL to deepen. Because entrainment also mixes warm, dry free atmosphere air with cloudy air, it causes on the other hand a drying of the ABL. This drying obviously causes the atmosphere to reach saturation at a higher altitude. If this entrainment increases, it is interesting to see whether the inversion height or the cloud base height increases more. A second effect is the longwave radiative cooling which cools the ABL, enhances turbulence and thus is a driving mechanism for entrainment.

At the surface, heat and moisture fluxes determine the amount of heat and moisture coming into the atmosphere, which is why they play an important role in the balance of the ABL.

Understanding the effect of large-scale conditions on the LWP by finding equilibrium solutions is the topic of this thesis.

1.3.1 GALES and the Mixed-Layer Model

To find equilibrium solutions of a Stratocumulus-Topped Boundary Layer (STBL), we use two models: the Mixed-Layer Model (MLM) and the GPU Accelerated Large Eddy Simulation (GALES). The MLM is a numerical model which provides a good understanding of the concepts of a STBL. However, we will see later that it has some limitations. GALES is based on the Dutch Atmospheric Large Eddy Simulation (Heus et al, 2010) and is a more accurate method to study the STBL than the MLM, because it handles the cloud dynamics in 3D. However, it requires much computational power but by the aid of a GPU this simulation can be accelerated a lot.

1.4 Outline

This thesis starts with an explanation of the thermodynamics involved in Sc clouds. Next some conservation laws will be applied. Then we will treat the two models: the LES and the Mixed Layer Model.

To obtain equilibrium solutions with GALES, we need a constant short-wave radiative forcing at the top of the atmosphere. To validate this method we will investigate in chapter 4 the effect of a diurnal cycle of the solar radiation as compared to a constant solar radiative forcing on the diurnally mean cloud thickness. The constant forcing has the same mean value as the mean solar radiation during a diurnal cycle. We will also check this for the *LWP* in a perturbed climate.

Using GALES, we do in chapter 5 idealized experiments of a set of large-scale conditions according to the CGILS framework, which includes a phase space consisting of the inversion jumps of temperature and specific humidity. We will also investigate the effect of a perturbed climate in which we increase the *SST* by 2 K.

To gain more insight in the physical concepts of Sc we will use in chapter 6 the MLM to investigate equilibrium states of a STBL. This includes the investigation of clear/cloudy ABL initial conditions.

In chapter 7 we quantify the effect of small perturbations of large-scale conditions on the thickness of the Sc.

In the last chapter the general conclusions and recommendations for future research will be presented.

Chapter 2

Theory

In this section I will outline the main principles needed to understand the physical processes that occur in a Stratocumulus Topped Boundary Layer (STBL). I will first treat some atmospheric thermodynamic principles and after that I will outline the governing equations that are needed to model the STBL.

2.1 Thermodynamics

This section describes the thermodynamics of a STBL. In stratocumulus clouds there are two conserved variables which are the most important, these are the liquid water potential temperature θ_l and the total specific humidity q_t , given by:

$$\theta_l = \theta - \frac{L_v q_l}{c_p \Pi}, \quad (2.1)$$

with $\Pi = \frac{T}{\theta}$, and

$$q_t = q_v + q_l. \quad (2.2)$$

This section describes the equations needed to determine these variables. For further detail see Wallace and Hobbs (2006) and De Roode (2004).

First of all the pressure can be expressed by the hydrostatic balance:

$$\frac{\partial p}{\partial z} = -\rho g, \quad (2.3)$$

where p is the pressure, ρ the density of air and g the gravitational acceleration. Secondly we need to describe the dry air in the atmosphere by using the Ideal gas law, which reads:

$$pV = nRT, \quad (2.4)$$

where p is the pressure of the gas, V the volume, and n is the amount of moles of the gas. R is the universal gas constant, which is equal to 8.3145

$\text{J K}^{-1} \text{ mol}^{-1}$, and T is the absolute temperature in Kelvin (K). (2.4) can also be written in terms of kilograms instead of moles, which gives:

$$pV = \frac{m_i}{M_i} RT. \quad (2.5)$$

Here the total mass of the gas is m_i and M_i is the molecular weight of a species i (g/mol). This molecular weight can be substituted out by using the specific gas constant R_i , which is defined as

$$R_i = \frac{R}{M_i}. \quad (2.6)$$

We can now define the apparent molecular weight M_d of dry air as the total mass of the constituent gases in dry air divided by the total number of moles of the constituent gases; that is,

$$M_d = \frac{\sum_i m_i}{\sum_i \frac{m_i}{M_i}} \quad (2.7)$$

The apparent molecular weight of dry air is 28.97 g/mol. Now we can calculate the gas constant for dry air R_d , which is

$$R_d = 1000 \frac{R}{M_d} = 1000 \frac{8.3145}{28.97} = 287.0 \text{ J K}^{-1} \text{ kg}^{-1}. \quad (2.8)$$

Dividing (2.5) by V , substituting $\rho = \frac{m_i}{V}$ and inserting (2.8) into (2.5) gives

$$p = \rho R_d T. \quad (2.9)$$

Now the potential temperature θ of an air parcel can be defined as the temperature that the parcel of air would have if it were expanded or compressed adiabatically from its existing pressure and temperature to a standard pressure p_0 (generally taken as 1000 hPa), which gives

$$\theta = T \left(\frac{p_0}{p} \right)^{\frac{R_d}{c_p}} = \frac{T}{\Pi}. \quad (2.10)$$

In other words an air parcel with temperature T and pressure p will have a potential temperature θ , which value would be equal to T_0 if that air parcel would be displaced to pressure p_0 .

The liquid water potential temperature θ_l is given by

$$\begin{aligned} \theta_l &= \theta \exp \left(- \frac{L_v q_l}{c_p T} \right) \\ &\approx \theta \left(1 - \frac{L_v q_l}{c_p T} \right) \\ &= \theta - \frac{L_v q_l}{c_p} \frac{\theta}{T}. \end{aligned} \quad (2.11)$$

We can further approximate this by using

$$\Pi = \left(\frac{p}{p_0} \right)^{\frac{R_d}{c_p}} = \frac{T}{\theta} \approx 1. \quad (2.12)$$

Then (2.11) reduces to

$$\theta_l \approx \theta - \frac{L_v}{c_p} q_l. \quad (2.13)$$

The lapse rate of the potential temperature can be obtained by differentiating (2.10) with respect to height:

$$\frac{d\theta}{dz} = \frac{\theta}{T} \left(\frac{dT}{dz} - \frac{R_d T}{p c_p} \frac{dp}{dz} \right). \quad (2.14)$$

By substitution of (2.3) and using (2.9), this can be written as

$$\frac{d\theta}{dz} = \frac{\theta}{T} \left(\frac{dT}{dz} + \frac{g}{c_p} \right). \quad (2.15)$$

From this it follows that when an air parcel follows the dry adiabatic lapse rate $\Gamma_d = dT/dz = -g/c_p$, then $d\theta/dz = 0$ and the potential temperature is constant with height. Due to this characteristic θ is a very convenient variable to work with. However, in the region where there are clouds θ would not be constant anymore because there is latent heat release in the clouds due to the condensation of water vapor. Because of that a correction for the latent heat release has to be made to keep θ constant, which is now the liquid water potential temperature θ_l , given by (2.1).

2.1.1 Moisture variables

In meteorology, one often uses dimensionless variables to measure the humidity of the air in terms of the ratio of the mass of water to either the mass of dry air, or its ratio to the mass of dry air and of water. The first one is called the mixing ratio, r , and the latter the specific humidity q ,

$$r_k = \frac{m_k}{m_d}, \quad q_k = \frac{m_k}{m} \quad \text{where } k \in v, l, i. \quad (2.16)$$

The indices 'v', 'l' and 'i' indicate water vapor, liquid water and water in the ice phase respectively. $m = m_t + m_d$ is the total mass of air including the total water $m_t = m_v + m_l + m_i$ and m_d is the mass of dry air. In analogy with the total mass m_t the total specific humidity q_t can be defined by

$$q_t = q_v + q_l + q_i, \quad (2.17)$$

and analogously for the mixing ratio. The specific humidity and the mixing ratio are related as:

$$q_v = \frac{r_v}{1 + r_v}, \quad r_v = \frac{q_v}{1 - q_v}. \quad (2.18)$$

Because in the atmosphere $q_v \approx 0.01$, it follows that $q_v \approx r_v$.

Sometimes we are interested in measuring the depth of a cloud. For this we define the liquid water path (LWP) which is the integral of the specific liquid water content,

$$LWP = \int_0^{z_{top}} \rho q_l dz \quad (2.19)$$

The LWP is an important quantity because it is related to the optical depth of the cloud, given by:

$$\tau = \frac{3LWP}{2\rho_l r_e}, \quad (2.20)$$

where ρ_l is the density of the liquid water in the cloud and r_e is the cloud droplet effective radius. Typical numbers for stratocumulus clouds for the LWP are about 0.150 kg m^{-2} . If we take a density of $\rho_l = 1000 \text{ kg m}^{-3}$ and a typical cloud droplet effective radius for stratocumulus of $r_e \approx 10 \mu\text{m}$, this would give an optical depth of $\tau = 22.5$. The cloud albedo can to a good approximation be calculated by Savic-Jovicic and Stevens (2007):

$$A_{\text{cld}} = \frac{\tau}{\tau + 6.8}, \quad (2.21)$$

which corresponds to a cloud albedo of about 0.7 if $\tau = 22.5$. This shows that the cloud layer has a significant impact on the amount of radiation that reaches the surface of the Earth.

2.1.2 The virtual (potential) temperature

In this section we will derive an expression that incorporates the effect of liquid water and water vapor on the density of air. Consequently we will define the virtual potential temperature.

Because the density of liquid water is about 1000 times larger than that of dry air, we may neglect the influence of liquid water and water vapor on the specific volume of air ($v_l = V_l/m_l = 1/\rho_l$), but we cannot neglect its effect on the density of air. The total mass of moist air is $m = m_d + m_l + m_v$, where m_d is the mass of dry air, m_l the mass of the liquid water and m_v the mass of water in the gas phase. The total volume the total mass would occupy is $V = V_g + V_l$, where V_g is the volume occupied by all the gases. Because $V_l \ll V_g$, it follows that $V \approx V_g$. We can then express the density of the mixture as

$$\rho = \frac{m}{V} = \frac{m_d + m_v + m_l}{V}. \quad (2.22)$$

If we now compare this density to the density of dry air, and use the definitions of the specific humidities (2.16), we get

$$\frac{\rho_d}{\rho} = \frac{m_d}{m_d + m_v + m_l} = 1 - q_v - q_l. \quad (2.23)$$

If we neglect the partial pressure of liquid water and use the ideal gas law to find the total pressure as a sum of the partial pressures of dry air ($p_d = \rho_d R_d T$) and water vapor ($e = \rho_v R_v T$), we get

$$p = p_d + e = \rho R_m T = \rho_d R_d T + \rho_v R_v T. \quad (2.24)$$

By using (2.23) we can express R_m as:

$$R_m = (1 - q_v - q_l) R_d + q_v R_v. \quad (2.25)$$

It would be convenient if we can use the dry air gas constant R_d for the gaseous mixture instead of R_m . To this end we have to define a virtual temperature T_v into the gas law:

$$p = \rho R_m T = \rho [(1 - q_v - q_l) R_d + q_v R_v] T = \rho R_d T_v, \quad (2.26)$$

where

$$T_v = (1 - (1 - \frac{1}{\epsilon}) q_t - q_l) T. \quad (2.27)$$

In this equation $\epsilon = R_d/R_v \approx 0.622$. Analogously to (2.10) we can define the virtual potential temperature as

$$\theta_v = \frac{T_v}{\Pi}. \quad (2.28)$$

So what is the relevance of the virtual temperature? If we split the p , ρ and T_v into a mean and fluctuating part, and insert this into the gas law (2.26) we obtain:

$$(\bar{p} + p') = (\bar{\rho} + \rho') R_d (\bar{T}_v + T'_v). \quad (2.29)$$

Applying Reynold's averaging gives:

$$\frac{\bar{p}}{R_d} = \bar{\rho} \bar{T}_v + \overline{\rho' T'_v}. \quad (2.30)$$

Because $\overline{\rho' T'_v} \ll \bar{\rho} \bar{T}_v$, (2.30) can be reduced to

$$\frac{\bar{p}}{R_d} \approx \bar{\rho} \bar{T}_v. \quad (2.31)$$

If we now subtract (2.31) from (2.29) we obtain the following expression for the fluctuating part:

$$\frac{p'}{R_d} = \bar{\rho}' T'_v + \rho' \bar{T}_v + \rho' T'_v. \quad (2.32)$$

Now we can divide this equation by (2.31):

$$\frac{p'}{\bar{p}} = \frac{\rho'}{\bar{\rho}} + \frac{T'_v}{\bar{T}_v} + \frac{\rho' T'_v}{\bar{\rho} \bar{T}_v}. \quad (2.33)$$

Because the pressure fluctuations are very small with respect to the average pressure and because the last term in the rhs consists of the product of two fluctuations, $\frac{p'}{p}$ and $\frac{\rho' T'_v}{\rho T_v}$ can be neglected. This results in the following expression:

$$\frac{T'_v}{T_v} = -\frac{\rho'}{\rho}. \quad (2.34)$$

By using the virtual potential temperature (2.28) we can also write

$$\frac{\theta'_v}{\theta_v} = -\frac{\rho'}{\rho}. \quad (2.35)$$

This is a very important relation because it relates density differences to virtual temperature differences. Buoyancy determines the vertical motions in the atmosphere which is being determined by differences in the density. Indeed an air parcel with a lower temperature compared to the environment has a higher density which means that it falls while an air parcel with a higher temperature than it's environment has a lower density which means that it rises. Density fluctuations are however hard to measure while temperature changes are not. So this means that with (2.35) also differences in buoyancy can be determined with the aid of the virtual temperature.

2.2 Governing equations

To get a clear understanding of the mechanics in the atmosphere we need to describe mass, momentum and energy using budget equations. Mass, momentum and energy are all conserved quantities. In this section we follow Van Driel (2010) to describe the budget equations.

2.2.1 Conservation of mass

In the atmosphere there is conservation of mass, because there is no mass created or destroyed. Because mass is conserved, we can write

$$\frac{\partial \rho}{\partial t} + \frac{\partial \rho u_j}{\partial x_j} = 0. \quad (2.36)$$

If we assume that air is incompressible, this reduces to

$$\frac{\partial u_j}{\partial x_j} = 0, \quad (2.37)$$

which is known as the continuity equation.

2.2.2 Conservation of momentum

The momentum equation describes the velocity field of a fluid like air. It consists of three equations, one for each direction (x,y and z). These equations are called the Navier-Stokes equations:

$$\rho \left(\frac{\partial u_i}{\partial t} + \frac{\partial u_j u_i}{\partial x_j} \right) = -\frac{\partial p}{\partial x_i} + \frac{\partial}{\partial x_j} \left(\mu \frac{\partial u_i}{\partial x_j} \right) + F_i. \quad (2.38)$$

Here p is the pressure, μ the dynamic viscosity of the fluid and F_i is the sum of the body forces acting on the system. In the atmosphere, two important body forces play a role which are the gravitation force and the Coriolis force due to the rotation of the Earth. The gravitational force can be described by $F_i^g = -\delta_{i3}\rho g$, where δ_{ij} is the Kronecker delta function, and is present to make sure the gravity term is only enabled in the equation for the z-direction.

The Coriolis force can be described by

$$F_i^C = -2\rho\epsilon_{ijk}\Omega_j u_k, \quad (2.39)$$

where ϵ_{ijk} is the Levi-Civita symbol and is equal to 1 if ϵ_{ijk} is ϵ_{123} , ϵ_{231} or ϵ_{312} , and is equal to -1 if ϵ_{ijk} is ϵ_{213} , ϵ_{321} or ϵ_{132} . If two or more indices are equal to each other $\epsilon_{ijk} = 0$. Ω_j is the angular velocity of the Earth. The Navier-Stokes equations can then be rewritten to

$$\rho \left(\frac{\partial u_i}{\partial t} + \frac{\partial u_j u_i}{\partial x_j} \right) = -\frac{\partial p}{\partial x_i} + \frac{\partial}{\partial x_j} \left(\mu \frac{\partial u_i}{\partial x_j} \right) - \delta_{i3}\rho g - 2\rho\epsilon_{ijk}\Omega_j u_k. \quad (2.40)$$

2.2.3 Conservation of heat/total water

In our GALES simulations (which is being discussed in Chapter 3) the variable being used representing heat is the liquid water potential temperature θ_l and the variable representing the total specific humidity is q_t . If we consider a control volume, the tendency of $\psi \in \{\theta_l, q_t\}$ can be described by using a balance of the fluxes coming in and out the control volume. To account for internal fluctuations we also include a source/sink term. The conservation equation is then given by

$$\frac{D\psi}{Dt} = \frac{\partial \psi}{\partial t} + \frac{\partial u_j \psi}{\partial x_j} = S_\psi. \quad (2.41)$$

Here the subscript j indicates tensor notation $(x_1, x_2, x_3) = (x, y, z)$. For the velocity u_j it denotes (u_x, u_y, u_z) . S_ψ represents the source/sink term, which would represent freezing, melting or radiation in the equation for θ_l and precipitation in the equation for q_t . In this research however we ignore freezing, melting and precipitation.

If we now decompose ψ into a mean part ($\bar{\psi}$) and fluctuating part (ψ') as $\psi = \bar{\psi} + \psi'$, apply Reynolds averaging and use the continuity equation of (2.37), we obtain the following general tendency equation:

$$\frac{\partial \bar{\psi}}{\partial t} = -\frac{\partial \overline{u'\psi'}}{\partial x} - \frac{\partial \overline{v'\psi'}}{\partial y} - \frac{\partial \overline{w'\psi'}}{\partial z} - \bar{u} \frac{\partial \bar{\psi}}{\partial x} - \bar{v} \frac{\partial \bar{\psi}}{\partial y} - \bar{w} \frac{\partial \bar{\psi}}{\partial z} + S_\psi. \quad (2.42)$$

In this equation the first three terms on the right hand side are the turbulent fluxes, the second three terms are the advection terms and the last term is the source term. This equation is not being used in GALES but proves to be valuable later on when the Mixed Layer Model will be discussed.

2.3 Turbulent Kinetic Energy (TKE)

Turbulent kinetic energy is an important quantity because it is a measure of the turbulent intensity. It is defined as

$$TKE = k = \frac{1}{2}(\overline{u'^2}) = \frac{1}{2}(\overline{u_1'^2} + \overline{u_2'^2} + \overline{u_3'^2}). \quad (2.43)$$

The TKE budget equation is given by Stull (1986):

$$\underbrace{\frac{\partial \bar{k}}{\partial t}}_{L_k} + \underbrace{\bar{U}_j \frac{\partial \bar{k}}{\partial x_j}}_{C_k} = \underbrace{\delta_{i,3} \frac{g}{\theta_v} (\overline{u'_i \theta'_v})}_{G_k} - \underbrace{\overline{u'_i u'_j} \frac{\partial \bar{U}_i}{\partial x_j}}_{P_k} - \underbrace{\frac{\partial \overline{u'_j k}}{\partial x_j}}_{D_{k,v}} - \underbrace{\frac{1}{\bar{\rho}} \frac{\partial \overline{u'_j p'}}{\partial x_i}}_{D_{k,p}} - \epsilon. \quad (2.44)$$

Here ϵ represents the rate of dissipation. The overbar means that we take the Reynolds Averaged part. The various terms have the following physical meaning:

- L_k - represents the local tendency of TKE
- C_k - describes the advection of TKE by the mean wind
- G_k - is the buoyant production/destruction term. It is a production or loss term depending on whether the heat flux $\overline{u'_i \theta'_v}$ is positive (during daytime over land) or negative (at night over land).
- P_k - is the shear production/destruction term.
- $D_{k,v}$ - represents the turbulent transport of TKE due to fluctuating velocity u'_j .
- $D_{k,p}$ - is the pressure correlation term that describes how TKE is redistributed due to fluctuating pressure p' .

Chapter 3

Modelling the STBL

In this research we study equilibrium states of Stratocumulus clouds. For this purpose we base our research on two different models: Large Eddy Simulation (LES) and the Mixed-Layer Model (MLM). In this chapter we will firstly discuss the LES, including the model of the incoming shortwave radiation. After that the Mixed-Layer Model will be discussed.

3.1 Large Eddy Simulation (LES)

The equations presented in section 2.2 can not be analytically solved. Therefore numerical methods are needed to solve the Navier-Stokes equations. To model the atmospheric boundary layer (ABL) we need to solve the eddies which determine the turbulent flow. Large eddies cascade successively to smaller eddies until the smallest Kolmogorov scale has been reached where the eddies dissipate. These eddies range from the lowest Kolmogorov scale (around 1 mm) to the highest scale on the order of the size of the ABL (1 km). The most accurate method for solving these eddies is DNS: Direct Numerical Simulation. This method however requires a gridsize of around 10^{18} points for a cubicle of 1 km^3 , which requires too much computational power making it numerically too expensive. Thus a different method has to be used.

In computational expense, LES lies between DNS and Reynolds-stress models, where unlike Reynolds-stress models the larger three-dimensional unsteady turbulent motions are directly represented. Therefore LES can be expected to be more accurate and reliable than Reynolds-stress models, but it remains much cheaper than DNS, where most of the computational effort is expended on the smallest dissipative motions.

The LES model tackles the problem of solving the eddies by dividing this problem into two parts.

The first part consists of the large eddies in the cubicle, which are assumed to be the most important because they contain almost all of the energy of

the system. This part is being calculated explicitly using Navier-Stokes and is restricted by the grid resolution.

The second part is the subgrid part, where the eddies which are smaller than the gridsize are modeled. By modelling the subgrid part, the high computational cost of explicitly representing the small-scale motions is avoided.

There are four conceptual steps in LES (Pope, 2000):

1. A *filtering* operation is defined to decompose a variable $\phi(\vec{x}, t)$ into a filtered (or resolved) component $\tilde{\varphi}(\vec{x}, t)$ and a residual (or subgrid-scale, SGS) component $\varphi'(\vec{x}, t)$.
2. The equations for the evolution of the filtered velocity field are derived from the Navier-Stokes equations. These equations are of the standard form, with the momentum equation containing the *residual-stress tensor* (or SGS stress tensor) that arises from the residual motions.
3. Closure is obtained by modelling the residual-stress tensor, most simply by an eddy-viscosity model.
4. The model filtered equations are solved numerically for $\tilde{\varphi}(\vec{x}, t)$, which provides an approximation to the large-scale motions in one realization of the turbulent flow.

3.1.1 The LES filtered equations

The general filtering operation that is being used in LES can be defined by

$$\tilde{\varphi}(\vec{x}, t) = \int G(\vec{r}, \vec{x}) \phi(\vec{x} - \vec{r}, t) d\vec{r}, \quad (3.1)$$

where the integration is over the entire domain. The filter function G is a sharp spectral filter which has a sharp cut-off in the Fourier space. It satisfies the normalization condition

$$\int G(\vec{r}, \vec{x}) d\vec{r} = 1. \quad (3.2)$$

For further detail on this filter function see (Pope, 2000).

The residual field is defined by

$$\varphi'(\vec{x}, t) = \phi(\vec{x}, t) - \tilde{\varphi}(\vec{x}, t), \quad (3.3)$$

so that the variable field can be decomposed as

$$\phi(\vec{x}, t) = \tilde{\varphi}(\vec{x}, t) + \varphi'(\vec{x}, t). \quad (3.4)$$

This decomposition appears analogous to Reynolds decomposition, but there are some important differences. The resolved part $\tilde{\varphi}$ is in this case not

only the mean motion, but the sum of the mean motion and the large-scale turbulence. The second difference is that the filtered residual component is not zero:

$$\tilde{\varphi}'(\vec{x}, t) \neq 0. \quad (3.5)$$

The filtering operation from (3.1) can be applied to the continuity equation: (2.36), the momentum equation: (2.40), and the equation for a conserved quantity: (2.41). From this we can obtain the filtered equations given by (3.6). The full description of this derivation can be found in Heus et al (2010).

$$\frac{\partial \tilde{u}_i}{\partial x_i} = 0, \quad (3.6a)$$

$$\frac{\partial \tilde{u}_i}{\partial t} = -\frac{\partial \tilde{u}_i \tilde{u}_j}{\partial x_j} - \frac{\partial \pi}{\partial x_i} + \frac{g}{\theta_0} \tilde{\theta}_v \delta_{i3} - 2\epsilon_{ijk} \Omega_j \tilde{u}_k - \frac{\partial \tau_{ij}}{\partial x_j}, \quad (3.6b)$$

$$\frac{\partial \tilde{\varphi}}{\partial t} = -\frac{\partial \tilde{u}_j \tilde{\varphi}}{\partial x_j} - \frac{\partial R_{u_j, \varphi}}{\partial x_j} + S_\varphi. \quad (3.6c)$$

In (3.6b), δ_{ij} is the Kronecker delta and the modified pressure is represented by

$$\pi = \frac{\tilde{p}}{\rho_0} + \frac{2}{3}e, \quad (3.7)$$

where $e = \frac{1}{2}(\widetilde{u_i u_i} - \tilde{u}_i \tilde{u}_i)$ is the subfilter-scale turbulence kinetic energy (SFS-TKE).

τ_{ij} is the deviatoric part of the subgrid momentum flux and is given by

$$\tau_{ij} = \widetilde{u_i u_j} - \tilde{u}_i \tilde{u}_j - \frac{2}{3}e. \quad (3.8)$$

The SFS scalar fluxes in (3.6c) are denoted by

$$R_{u_j, \varphi} \equiv \widetilde{u_j \varphi} - \tilde{u}_j \tilde{\varphi}. \quad (3.9)$$

3.1.2 Subfilter-scale model

In GALES, the eddy diffusivity of the scalar flux is modelled using one and a half order closure (Heus et al, 2010):

$$R_{u_j, \phi} = -K_h \frac{\partial \tilde{\varphi}}{\partial x_j}, \quad (3.10)$$

where K_h is the eddy diffusivity coefficient. The subfilter scale stress tensor is given by

$$\tau_{ij} = -K_m \left(\frac{\partial \tilde{u}_i}{\partial x_j} + \frac{\partial \tilde{u}_j}{\partial x_i} \right), \quad (3.11)$$

α	c_f	$c_{\varepsilon,1}$	$c_{\varepsilon,2}$	c_m	$c_{h,1}$	$c_{h,2}$	c_N
1.5	2.5	0.19	0.51	0.12	1	2	0.76

Table 3.1: An overview of the parameters used in the SFS scheme of DALES/GALES.

where K_m is the eddy viscosity. These eddy diffusivity coefficients are a function of the SFS-TKE e . The prognostic equation for e is given by Deardorff (1980):

$$\underbrace{\frac{\partial e}{\partial t}}_{L_e} = - \underbrace{\frac{\partial \tilde{u}_j e}{\partial x_j}}_{C_e} - \underbrace{\tau_{ij} \frac{\partial \tilde{u}_i}{\partial x_j}}_{P_e} + \underbrace{\frac{g}{\theta_0} R_{w,\theta_v}}_{G_e} - \underbrace{\frac{\partial R_{u_j,e}}{\partial x_j}}_{D_{e,u}} - \underbrace{\frac{1}{\rho_0} \frac{\partial R_{u_j,\pi}}{\partial x_j}}_{D_{e,\pi}} - \varepsilon, \quad (3.12)$$

with ε the SFS-TKE dissipation rate. The various terms in (3.12) have the following physical meaning (Van Driel, 2010):

- L_e - the local change in time of e
- C_e - the convective transport of e
- P_e - the production/destruction of e due to shear
- G_e - the production/destruction of e due to buoyancy
- $D_{e,u}$ - the diffusive transport of e due to the velocity u_j
- $D_{e,\pi}$ - the diffusive transport of e due to pressure

This equation can be closed by using the parametrizations of (3.10) and (3.11) in (3.12). This results in the following equation (Heus et al, 2010):

$$\begin{aligned} \frac{\partial e}{\partial t} + \tilde{u}_j \frac{\partial e}{\partial x_j} = & K_m \left(\frac{\partial \tilde{u}_j}{\partial x_i} + \frac{\partial \tilde{u}_i}{\partial x_j} \right) \frac{\partial \tilde{u}_i}{\partial x_j} - K_h \frac{g}{\theta_0} \frac{\partial (A\tilde{\theta}_l + B\tilde{q}_t)}{\partial z} \\ & + \frac{\partial}{\partial x_j} \left(2K_m \frac{\partial e}{\partial x_j} \right) - \frac{c_\varepsilon e^{3/2}}{\lambda}. \end{aligned} \quad (3.13)$$

If the air is saturated, $A = A_w \approx 0.5$ and $B = B_w \approx 1000$ K are the moist coefficients. If the air is unsaturated, $A = A_d \approx 1.01$ and $B = B_d \approx 180$ K are the dry coefficients. The constants needed to model K_m and K_h are shown in Table 3.1.

3.1.3 Model of the incoming solar radiation

In this thesis the influence of the diurnal cycle of solar radiation as opposed to a diurnally averaged solar radiation will be investigated. To this end, we need a model of the incoming shortwave radiation. This section elaborates

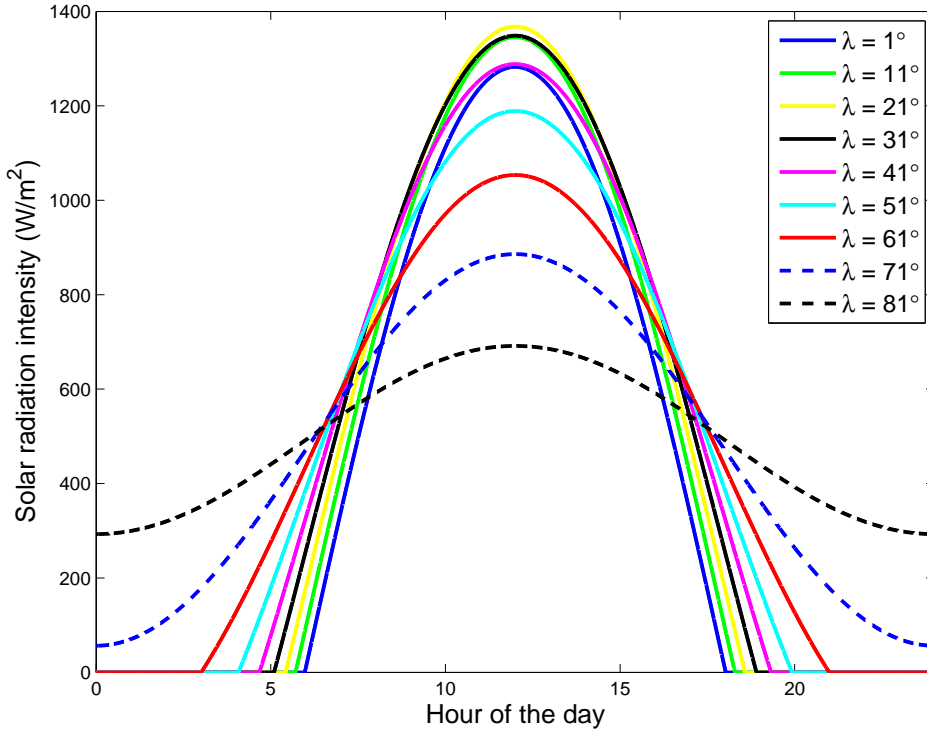


Figure 3.1: The solar irradiation at the top of the atmosphere plotted against time for different latitudes on 16 July.

on finding expressions for the solar intensity at the top of the atmosphere, which is being applied in GALES.

The intensity of the sun depends on the Zenith angle β as

$$I = I_0 \cos(\beta), \quad (3.14)$$

where $I_0 = 1368 \text{ W/m}^2$ is the solar constant (Woan, 2003). This Zenith angle is depending on the latitude λ , declination δ , and hour angle ωt as (Boeker and Van Grondelle, 1999):

$$\cos(\beta) = \sin(\lambda) \sin(\delta) + \cos(\lambda) \cos(\delta) \cos(\omega t). \quad (3.15)$$

The declination δ , which depends on the date, is defined as the latitude where the sun is at its zenith at noon. In the summer on 21 June this zenith would be 23.45° north of the equator and in the winter on 21 December it would be 23.45° south of the equator. The declination can be calculated using (3.16):

$$\sin(\delta) = \sin(\varepsilon) \sin\left(\frac{2\pi}{365.24}(N + 284)\right), \quad (3.16)$$

where N is the day of the year starting from the 1st of January and $\varepsilon = 23.45^\circ$ is the inclination of the earth.

The angular frequency ω can be calculated by

$$\omega = \frac{2\pi}{T_{\text{day}}} \text{ rad s}^{-1}, \quad (3.17)$$

where $T_{\text{day}} = 60 \times 60 \times 24 = 86400 \text{ s}$. The times of dawn ($-T$) and sunset ($+T$) are given by $\cos \beta = 0$, which leads to

$$\cos(\omega T) = -\tan \lambda \tan \delta. \quad (3.18)$$

In Figure 3.1 the solar irradiation I during a day is plotted to show the effect of latitude on 16 July. It can be seen that for high latitudes, $\lambda = 71^\circ$ or $\lambda = 81^\circ$, there will be daylight for 24 hours.

This solar radiation intensity can be averaged over one day to a constant irradiation using (3.19):

$$\langle I \rangle = \frac{1}{T_{\text{day}}} \int_0^{T_{\text{day}}} I(t) dt. \quad (3.19)$$

If we use for example a latitude of $\lambda = 32^\circ$, this would result in $\langle I \rangle = 486 \text{ W/m}^2$.

3.2 The Mixed-Layer Model

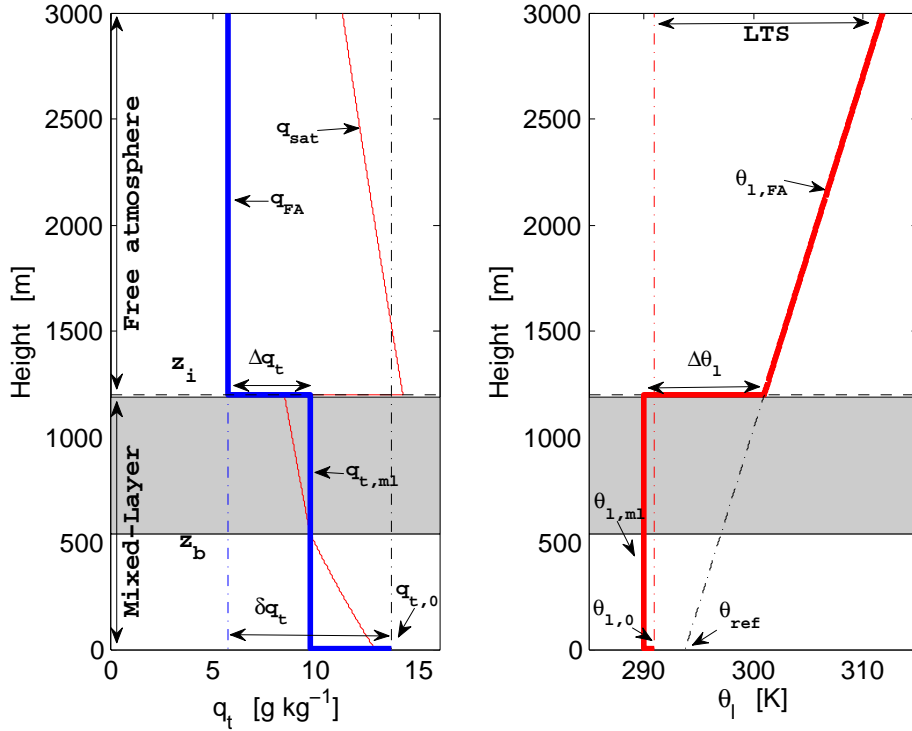


Figure 3.2: Typical q_t and θ_l profiles for a STBL. In the left plot the red line marks the saturated specific humidity q_{sat} . At the point of intersection between q_{sat} and $q_{t,ml}$ the cloud base z_b is found. The cloudy region is shaded gray.

θ_{ref} is $\theta_{l,FA}$ extrapolated to the surface and $LTS = \theta_l(z = 3000 \text{ m}) - \theta_{l,0}$ is the Low Tropospheric Stability.

In order to get a better understanding of Sc I will now introduce the Mixed-Layer Model (MLM). This model assumes that the boundary layer is

vertically well mixed, that means that the conserved variables are constant with height up to the boundary layer height z_i . We also assume that the mean values of the conserved variables are homogeneous in the horizontal directions (x,y). If we apply these assumptions to (2.42) we obtain the following equation:

$$\frac{\partial \bar{\psi}}{\partial t} = -\frac{\partial \overline{w'\psi'}}{\partial z} + \overline{S_\psi}. \quad (3.20)$$

If the vertical gradient of any mean variable $\psi \in \{q_t, \theta_l\}$ does not change with time, we can write

$$\frac{\partial}{\partial z} \left(\frac{\partial \bar{\psi}}{\partial t} \right) = 0. \quad (3.21)$$

This situation is also called a quasi-steady state. If we now consider (3.20) and assume that there is no source/sink term (precipitation, radiation), then the tendency of $\bar{\psi}$ will be determined by the vertical gradient of the turbulent flux:

$$\frac{\partial \bar{\psi}}{\partial t} = -\frac{\partial \overline{w'\psi'}}{\partial z}. \quad (3.22)$$

Inserting this into (3.21) gives

$$\frac{\partial}{\partial z} \left(\frac{\partial \bar{\psi}}{\partial t} \right) = -\frac{\partial^2 \overline{w'\psi'}}{\partial z^2} = 0, \quad (3.23)$$

which implies that the vertical gradient of the turbulent flux is constant:

$$\frac{\partial \overline{w'\psi'}}{\partial z} = \text{constant}. \quad (3.24)$$

If we integrate this equation and apply the boundary conditions

$$\overline{w'\psi'}(z=0) = \overline{w'\psi'_0}, \quad (3.25)$$

$$\overline{w'\psi'}(z=z_i^-) = \overline{w'\psi'_T}, \quad (3.26)$$

where z_i^- denotes the height just beneath the inversion (the inversion is a discontinuity), and where $\overline{w'\psi'_0}$ and $\overline{w'\psi'_T}$ are the turbulent fluxes at the surface and cloud top respectively, we can obtain the following equation for the turbulent flux:

$$\overline{w'\psi'} = \overline{w'\psi'_0} \left(1 - \frac{z}{z_i}\right) + \overline{w'\psi'_T} \frac{z}{z_i}. \quad (3.27)$$

The surface flux $\overline{w'\psi'_0}$ can be parameterized as

$$\overline{w'\psi'_0} = C_D |\vec{U}| (\psi_0 - \psi_{ml}), \quad (3.28)$$

where $C_D \approx 0.001$ is an exchange coefficient and $|\vec{U}|$ is the absolute horizontal wind velocity relative to the surface. ψ_{ml} and ψ_0 are the values in the

mixed layer and at the surface respectively. Figure 3.2 shows the vertical profiles of ψ .

$\overline{w'\psi'_T}$, the turbulent flux at the top, is being controlled by the rate of mixing of free atmospheric air above z_i with cloudy air just below z_i and by the size of the inversion jump. This rate of mixing is called the entrainment w_e . If we consider an infinitesimally thin inversion layer this relation for the turbulent flux at the top can be described by

$$\begin{aligned}\overline{w'\psi'_T} &= -w_e\Delta\psi \\ &= -w_e(\psi_{fa}(z_i^+) - \psi_{ml}),\end{aligned}\tag{3.29}$$

where $\psi_{fa}(z_i^+)$ is the value of ψ in the free atmosphere just above the inversion jump. The entrainment rate gives also the rate with which the boundary layer height grows in time:

$$\frac{dz_i}{dt} = \bar{w} + w_e,\tag{3.30}$$

where \bar{w} is the large scale subsidence which is pushing down on the boundary layer. The large scale subsidence \bar{w} can be determined by using the continuity equation for incompressible flow, which reads

$$\frac{\partial\bar{u}}{\partial x} + \frac{\partial\bar{v}}{\partial y} + \frac{\partial\bar{w}}{\partial z} = 0.\tag{3.31}$$

$\frac{\partial\bar{u}}{\partial x} + \frac{\partial\bar{v}}{\partial y} = D$, where D is the divergence, and if it is a constant, then it follows that

$$\frac{\partial\bar{w}}{\partial z} = -\left(\frac{\partial\bar{u}}{\partial x} + \frac{\partial\bar{v}}{\partial y}\right) = -D.\tag{3.32}$$

Integrating this equation over z gives

$$\bar{w} = -Dz.\tag{3.33}$$

From this equation it can be concluded that the subsidence increases linearly with height if D is a constant, otherwise not.

The source/sink term S_ψ from (3.20) usually represent precipitation, or shortwave and longwave radiation. In this thesis precipitation is ignored so that means that $S_q=0$. So only shortwave radiation and longwave radiation need to be described. S_θ can be described as

$$S_\theta = -\frac{1}{\rho_0 c_p} \frac{\partial F}{\partial z},\tag{3.34}$$

where

$$F = L \uparrow - L \downarrow + S \uparrow + S \downarrow + F_0.\tag{3.35}$$

Here $L \uparrow$ and $L \downarrow$ denote the upward and downward longwave radiative fluxes, and $S \uparrow$ and $S \downarrow$ the upward and downward shortwave radiative

fluxes. F_0 is a height-independent reference value chosen for convenience to make F zero in the subcloud layer because only the flux divergence within the cloud layer is of importance, rather than the absolute value. Integrating (3.34) over the boundary layer (0 to z_i) gives

$$\int_0^{z_i} S_\theta dz = -\frac{1}{\rho_0 c_p} dF. \quad (3.36)$$

dF represents the difference between the radiative flux at the top and the surface of the boundary layer.

If we now integrate (3.20) from 0 to z_i and apply the boundary conditions from (3.28) and (3.29) and assume that the tendencies for \bar{q}_t and $\bar{\theta}_l$ are independent of height we can obtain the following equations for $q_{t,ml}$ and $\theta_{l,ml}$, which are bulk values:

$$z_i \frac{dq_{t,ml}}{dt} = C_D |\vec{U}| (q_{t,0} - q_{t,ml}) + w_e \Delta q_t, \quad (3.37a)$$

$$z_i \frac{d\theta_{l,ml}}{dt} = C_D |\vec{U}| (\theta_{l,0} - \theta_{l,ml}) + w_e \Delta \theta_l - \frac{1}{\rho_0 c_p} dF. \quad (3.37b)$$

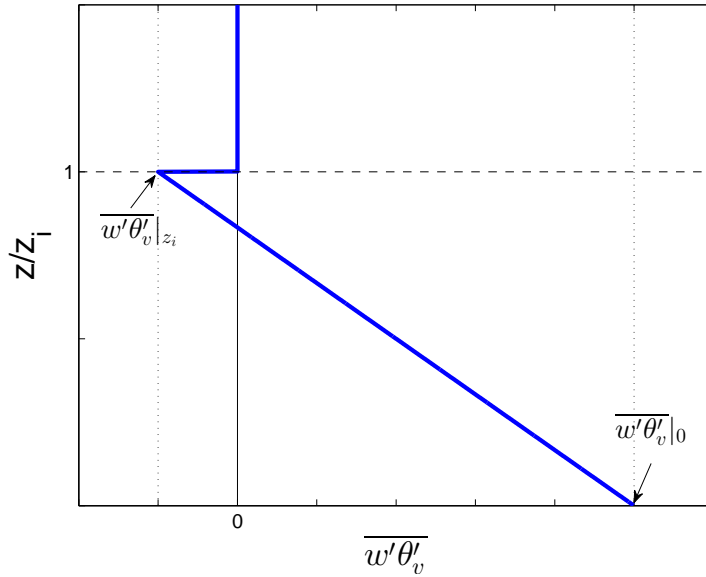


Figure 3.3: Typical virtual potential temperature flux profile for a CBL.

3.2.1 Entrainment in a clear boundary layer

We will see later in this study that we also encounter the break up of Sc, leading to a Clear Convective Boundary Layer (CBL) and we also study equilibrium states of an initially CBL. For the time evolution of a CBL we need an expression for the entrainment in a CBL.

In a clear convective boundary layer the turbulent flux $\overline{w'\theta'_v}|_{z_i}$ at the cloud top is found to be dependent only on the surface flux given by Stull (1986):

$$\overline{w'\theta'_v}|_{z_i} = -A_{\theta_v} \overline{w'\theta'_v}|_0, \quad (3.38)$$

where $A_{\theta_v} \approx 0.2$ is the entrainment flux ratio. A typical flux profile for a CBL is shown in Figure 3.3.

By using (3.28),(3.29) and (3.38) the following expression for the entrainment in a clear boundary layer can be obtained:

$$\begin{aligned} w_e &= A_{\theta_v} \frac{C_D U (\theta_{v,0} - \theta_{v,ml})}{\Delta\theta_v} \\ &= A_{\theta_v} \frac{C_D U (\theta_{v,0} - \theta_{v,ml})}{\theta_{v,fa}(z_i^+) - \theta_{v,ml}} \end{aligned} \quad (3.39)$$

In accord with Figure 3.2 we express $\theta_{FA}(z)$, which is the potential temperature above the inversion, as

$$\theta_{FA}(z) = \theta_{ref} + \Gamma_{\theta} z \quad \text{for } z > z_i, \quad (3.40)$$

where θ_{ref} is the extrapolated potential temperature from just above the inversion to the surface and Γ_{θ} is the potential temperature lapse rate.

Since in a clear atmosphere there is no liquid water, the virtual potential temperature reads

$$\theta_v = \theta(1 + \epsilon_I q_v), \quad (3.41)$$

where

$$\epsilon_I = \frac{1}{\epsilon} - 1 \approx 0.61. \quad (3.42)$$

Using (3.41), and using the fact that $q_v = q_t$ (since there is no liquid water), it follows from (3.40) that

$$\theta_{v,fa}(z) = (\theta_{ref} + \Gamma_{\theta} z)(1 + \epsilon_I q_{t,fa}) \quad \text{for } z > z_i, \quad (3.43)$$

and

$$\theta_{v,ml} = \theta_{ml}(1 + \epsilon_I q_{t,ml}) \quad \text{for } 0 < z < z_i. \quad (3.44)$$

3.2.2 Entrainment in a STBL

For a stratocumulus topped boundary layer (STBL) we need to take into account the effect of the radiative cooling on the entrainment. Therefore some parametrizations are created to deal with this complex quantity.

One of the most simple entrainment parametrizations is Moeng's (Moeng, 2000):

$$\begin{aligned} w_e &= \frac{A_{\theta_v} \overline{w'\theta'_{l,0}} + A_1 F'}{\Delta\theta_l} \\ &= \frac{A_{\theta_v} C_{DU}(\theta_{l,0} - \theta_{l,ml}) + A_1 F'}{\theta_{ref} + \Gamma_{\theta} z_i - \theta_{l,ml}}. \end{aligned} \quad (3.45)$$

Here A_1 is given by

$$A_1 = (2.5 - 2e^{-\sqrt{b_m LWP}})(1 - e^{-\kappa \cdot LWP}), \quad (3.46)$$

where $b_m = 0.9 \text{ m}^2/\text{kg}$ and $\kappa = 130 \text{ m}^2/\text{kg}$ is the longwave absorption coefficient. $F' = \frac{dF_L}{\rho_0 c_p}$ where dF_L is the longwave radiative flux divergence of the cloud top. A typical value of dF_L for Sc is 70 W/m^2 . For the density ρ_0 we choose a constant value of $\rho_0 = 1.14 \text{ kg/m}^3$. To clarify (3.46), the entrainment efficiency factor A_1 is plotted versus the LWP in Figure 3.5. It shows that A_1 increases exponentially with the LWP . The physical reason for this is that in the case of a thick cloud, the depth over which the buoyancy flux is positive becomes larger, which has the consequence that there is more TKE production and more entrainment.

The adiabatic LWP for stratocumulus clouds can be expressed as (Stull, 1986):

$$LWP = \frac{1}{2} \rho_0 \Gamma_{q_l} (z_i - z_b)^2, \quad (3.47)$$

A typical value of the liquid water lapse rate is $\Gamma_{q_l} \approx 2 \cdot 10^{-6} \text{ kgkg}^{-1}\text{m}^{-1}$.

An example of the entrainment rate as a function of the inversion jump $\Delta\theta_l$ for some typical values of the variables in (3.45) can be seen in Figure 3.4. It can be observed that the entrainment rate decreases as the inversion jump at the boundary layer top increases. Another thing that can be observed is that the entrainment rate is much higher in a STBL than in a clear boundary layer, which is a result of the longwave radiative cooling at the cloud top.

3.2.3 Cloud-top entrainment instability (CTEI)

We know from (2.44) that

$$\frac{\partial \bar{k}}{\partial t} \simeq \frac{g}{\theta_0} \overline{w'\theta'_v}. \quad (3.48)$$

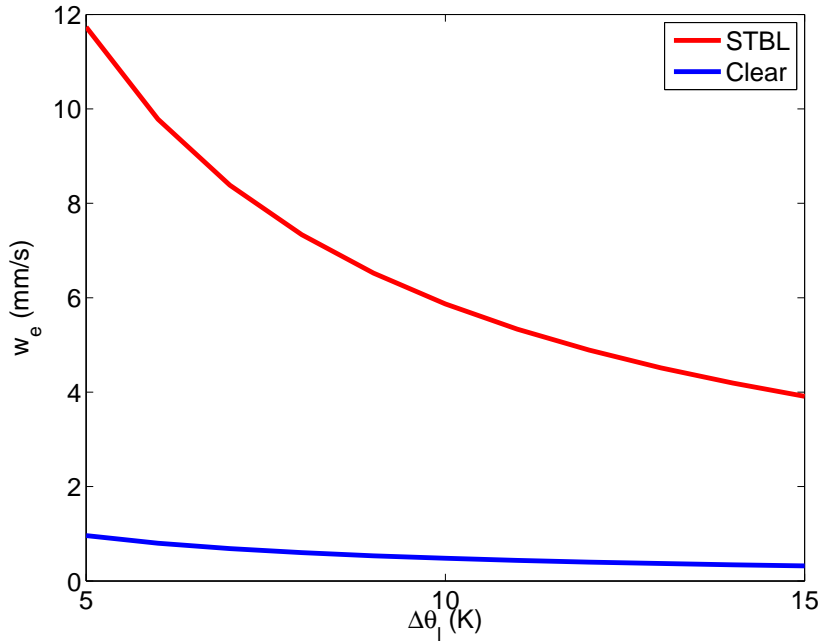


Figure 3.4: The entrainment w_e as a function of the inversion jump $\Delta\theta_l$ for the clear boundary layer and for the STBL using Moeng's parametrization. The parameters used are $\theta_{l,0} = 292$ K, $\theta_{l,ml} = 289$ K, $U = 8$ m/s and for the STBL the $LWP = 50$ g/m². As the difference is small, we use for simplicity the approximation $\overline{w'\theta'_{l,0}} \approx \overline{w'\theta'_{v,0}}$

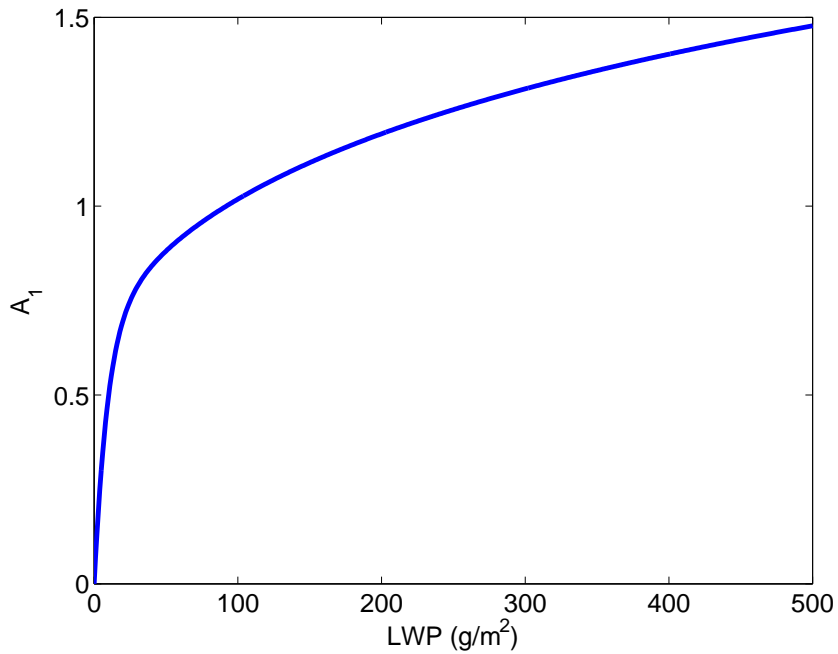


Figure 3.5: Factor A_1 plotted versus the LWP .

At the cloud top, entrainment causes the downward movement of warm free atmosphere air. This means that $w' < 0$, $\theta'_v > 0$ and $\frac{\partial \bar{k}}{\partial t} < 0$. However, this mixing of warm, dry free atmosphere air with colder, moist ABL air also causes the evaporation of liquid water droplets which cools the ABL air. It is possible that under certain conditions this evaporative cooling more than compensates for the warming due to entrainment such that $\theta'_v < 0$. The result of these effects combined is that $\overline{w'\theta'_v} > 0$ (buoyancy reversal). This process is called *cloud-top entrainment instability* (CTEI). Due to entrainment more *TKE* is being generated which leads to more *TKE* and consequently more entrainment. This is an unstable situation. It has been suggested that this high entrainment can lead to a rapid dissipation of the Sc cloud (Randall, 1980) and (Deardorff, 1980).

Following De Roode (2004) the buoyancy flux in the cloud layer can be written as

$$\overline{w'\theta'_v} = A_w \overline{w'\theta'_l} + B_w \overline{w'q'_t}, \quad (3.49)$$

with moist coefficients $A_w \approx 0.5$ and $B_w \approx 1000$ K. If we insert this equation into (3.29) we obtain

$$\overline{w'\theta'_v}|_T = A_w \overline{w'\theta'_l}|_T + B_w \overline{w'q'_t}|_T = -w_e (A_w \Delta \bar{\theta}_l + B_w \Delta \bar{q}_t). \quad (3.50)$$

If

$$\Delta \bar{\theta}_l < -\frac{B_w}{A_w} \Delta \bar{q}_t, \quad (3.51)$$

the buoyancy flux due to entrainment becomes positive. For $\Delta \bar{q}_t$ in g/kg, $B_w/A_w \approx 2$ K/(g/kg).

3.2.4 Steady-state

Mixed-Layer

In this research the main emphasis is finding steady-state solutions of the STBL. To reach a steady-state, we need to have an equilibrium of three quantities in the mixed layer: $\theta_{l,ml}$, $q_{t,ml}$ and z_i . Furthermore we need a steady-state in the free atmosphere, which is the region above the boundary layer. This section elaborates on finding steady-state expressions for the quantities in the mixed layer.

In a steady-state (3.20) can be rewritten as

$$0 = -\frac{\partial \overline{w'\psi'}}{\partial z} + \overline{S_\psi}. \quad (3.52)$$

This equation states that in a steady-state the turbulent flux gradient should balance the source term. Using the mixed layer equations, (3.37a) and (3.37b), we find the following expressions for a steady-state:

$$C_D |\vec{U}| (q_{t,0} - q_{t,ml}) = -w_e \Delta q_t \quad (3.53)$$

and

$$C_D|\vec{U}|(\theta_{l,0} - \theta_{l,ml}) = -w_e\Delta\theta_l + \Delta F_L, \quad (3.54)$$

with

$$\Delta F_L = (1 - e^{-\kappa \cdot LWP})F'. \quad (3.55)$$

In the limit of $LWP \rightarrow \infty$, ΔF_L converges to F' . To clarify (3.53) and (3.54), the typical flux profiles of $\overline{w'q'_t}$ and $\overline{w'\theta'_l}$ are shown in Figure 3.6.

If we use the relationship $\Delta\psi = \psi_{fa} - \psi_{ml}$, and use (3.40), we can solve (3.53) and (3.54) for ψ_{ml} . This gives:

$$\theta_{l,ml} = \theta_{l,0} + \frac{w_e(\theta_{ref} + \Gamma_\theta z_i - \theta_{l,0}) - \Delta F_L}{C_D|\vec{U}| + w_e}, \quad (3.56a)$$

$$q_{t,ml} = q_{t,0} + \frac{w_e(q_{t,fa} - q_{t,0})}{C_D|\vec{U}| + w_e}. \quad (3.56b)$$

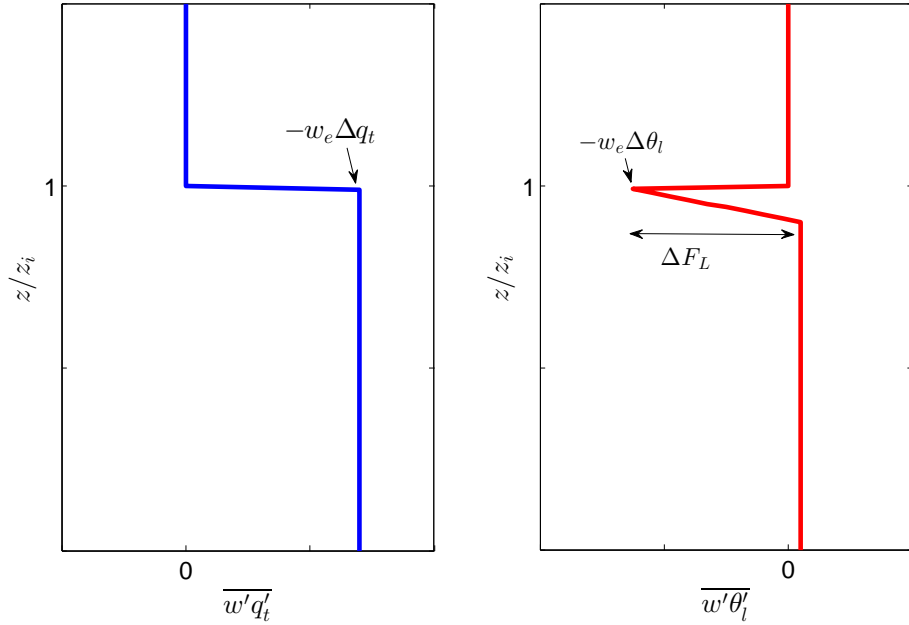


Figure 3.6: Typical steady-state moisture and liquid water potential temperature flux profiles for a STBL.

From these equations it can be seen that an increase of entrainment rate w_e corresponds with heating of the mixed layer, because warmer air in the free atmosphere just above the inversion height z_i is being mixed with colder air in the mixed layer. An increase in w_e in the equation for $q_{t,ml}$ corresponds with a drying of the mixed layer, because dryer air from just above the inversion is being mixed with moister air in the mixed layer.

What can also be observed is that an increased wind speed results in a cooler and moister mixed layer.

The third equation we need is the equilibrium of z_i . From (3.30) it follows that in steady-state we have a balance between entrainment that tends to heighten the boundary layer and subsidence that pushes it down:

$$w_e = -\bar{w}, \quad (3.57)$$

which in the case of a linearly increasing subsidence results in:

$$w_e = Dz_i. \quad (3.58)$$

The free atmosphere

In addition to reaching a steady-state in the mixed layer, we also need to reach a steady-state in the free atmosphere (FA). There are two conditions which have to be met, that is, a steady-state of $q_{t,fa}$ and a steady-state of $\theta_{l,fa}$. $\theta_{l,fa}$ is defined by (3.40) and $q_{t,fa}$ can be defined as

$$q_{t,fa} = q_{t,0} + \delta q_t + \Gamma_q z \quad \text{for } z > z_i. \quad (3.59)$$

$q_{t,0}$ is the saturated specific humidity at the sea surface. If we take for example a $SST = 288$ K and pressure $p = 1012.5$ hPa we will have a $q_{t,0} = 10.5$ g/kg. δq_t is related to the inversion jump of specific humidity at the inversion height. The values of $q_{t,fa}$ depend on the actual environmental conditions. To prevent negative values of the specific humidity in the free atmosphere, δq_t would typically range in this case from $\delta q_t \in [-2, -10]$ g/kg.

The third term in (3.59) is the vertical lapse rate. In this research we will mainly focus on a zero lapse rate, $\Gamma_q = 0$, but also a lapse rate of $\Gamma_q < 0$ will be considered.

To obtain the tendency equation for ψ_{fa} we need to use (2.42). In the free atmosphere there is no turbulence. That means that the turbulent terms on the right hand side of (2.42) are zero, from which it follows that

$$\frac{\partial \bar{\psi}}{\partial t} = -\bar{u} \frac{\partial \bar{\psi}}{\partial x} - \bar{v} \frac{\partial \bar{\psi}}{\partial y} - \bar{w} \frac{\partial \bar{\psi}}{\partial z} + S_\psi. \quad (3.60)$$

The source term in (3.60) is as before only relevant for the temperature equation, where it acts as the radiative cooling of the atmosphere. Furthermore it is assumed that there is a horizontal homogeneity which means that the horizontal advection terms in (3.60) drop out. If we apply this budget equation to the free atmosphere, the resulting tendency equations for q_t and θ_l are then given by

$$\frac{\partial q_t}{\partial t} = -\bar{w} \Gamma_q \quad \text{and} \quad (3.61a)$$

$$\frac{\partial \theta_l}{\partial t} = -\bar{w} \Gamma_\theta - \frac{1}{\rho(z)c_p} \frac{\partial F}{\partial z}. \quad (3.61b)$$

It can be seen from (3.61a) that when $\Gamma_q < 0$, together with the fact that $\bar{w} < 0$, that $\frac{\partial q_t}{\partial t} < 0$. If there is a lapse rate in q_t there will be *subsidence drying* of the free atmosphere. Because we study steady-state solutions it is important that the lapse rate $\Gamma_q = 0$ or we need a balancing advection term to make $\frac{\partial q_t}{\partial t} = 0$.

To maintain a constant θ_l , we need a balance between *subsidence warming* and radiative cooling:

$$-\bar{w}\Gamma_\theta = \frac{1}{\rho(z)c_p} \frac{\partial F}{\partial z}. \quad (3.62)$$

In this case a non zero temperature lapse rate does seem to be more realistic and this is indeed also found in nature. For research purposes this radiative cooling will be modified if necessary to maintain a constant free atmosphere temperature.

3.2.5 Determining the cloud base height in the MLM

To obtain the cloud layer depth (or *LWP*) we need to determine the cloud base height. This section will explain in several steps how the cloud base height can be obtained. First of all, we need an expression of the pressure as a function of height ($p(z)$). Under vertically well mixed subcloud layer conditions $\theta_{v,subcloud} = \text{constant}$. By using

$$\frac{d\theta_v}{dz} = \frac{dT_v}{dz} + \frac{g}{c_p} = 0, \quad (3.63)$$

T_v can be written as

$$T_v = T_{v,0} - \frac{g}{c_p}z, \quad (3.64)$$

where $T_{v,0}$ is the lowest value of the virtual temperature in the atmosphere. By using (2.28), this equation can be rewritten to

$$\left(\frac{p}{p_0}\right)^{R_d/c_p} \theta_v = \left(\frac{p_s}{p_0}\right)^{R_d/c_p} \theta_v - \frac{g}{c_p}z. \quad (3.65)$$

Dividing this equation by θ_v and multiplying by $p_0^{R_d/c_p}$ gives

$$p^{R_d/c_p} = p_s^{R_d/c_p} - \frac{gp_0^{R_d/c_p}z}{c_p\theta_v}. \quad (3.66)$$

This equation can then be rewritten to obtain an expression for the pressure:

$$p(z) = \left(p_s^{R_d/c_p} - \frac{gp_0^{R_d/c_p}z}{c_p\theta_v} \right)^{c_p/R_d}. \quad (3.67)$$

Secondly we need an expression for the saturation vapor pressure $e_s(z)$. Using the definition of the Exner function:

$$\Pi(z) = \left(\frac{p_0}{p(z)} \right)^{-R_d/c_p}, \quad (3.68)$$

we have for $T(z)$:

$$T(z) = \Pi(z)\theta_{t,ml}. \quad (3.69)$$

The saturation vapor pressure is to a good approximation given by Stull (1986):

$$e_s(z) = 0.61078 \cdot 10^3 \cdot \exp\left(\frac{17.27(T(z) - 273.16)}{T(z) - 35.86}\right). \quad (3.70)$$

Now the saturation specific humidity $q_s(z)$ can be evaluated as:

$$q_s(z) = \frac{R_d}{R_v} \frac{e_s(z)}{p(z) - e_s(z)}. \quad (3.71)$$

Using this formula we can iterate for increasing z and we find z_b at the point that $q_s = q_{t,ml}$.

Chapter 4

EUROCS: GALES results of the stratocumulus case

The EUROpean Cloud Systems (EUROCS) project used observations made of stratocumulus clouds off the coast of California during FIRE I. The measurements of FIRE I started on 14 July 1987, on San Nicolas Island (33.15°, -119.50°). For further detail see Duynkerke et al (2004).

To study equilibrium states of Sc with GALES, we need a constant radiative forcing instead of a diurnal cycle of the solar radiative forcing. This constant radiative forcing is the same as the mean value of the diurnal cycle of the radiation. To justify the use of a constant radiative forcing, we firstly use GALES on the EUROCS case to check whether this diurnal cycle of the solar radiation works correctly and is in agreement with the EUROCS results from Duynkerke et al (2004) and secondly we use GALES to validate the use of a constant diurnally averaged solar radiation. This will be done by comparing the mean *LWP* of both methods. We also aim to study the response of the cloud system to perturbations in the sea surface temperature (SST). In this perturbed climate we also need to validate the use of a constant diurnally averaged radiation.

4.1 Setup

4.1.1 Initial and boundary conditions

The initial profiles for the EUROCS case are prescribed by:

$$\begin{array}{l} 0 < z \leq 595 \text{ m} \\ 595 < z \leq 1200 \text{ m} \end{array} \quad \begin{cases} \theta_l = 287.5 & (\text{K}) \\ q_t = 9.6 & (\text{g kg}^{-1}) \\ \theta_l = 299.5 + 0.0075(z - 595) & (\text{K}) \\ q_t = 6.6 - 0.003(z - 595) & (\text{g kg}^{-1}) \end{cases} \quad (4.1)$$

The sea surface temperature (SST) and pressure are prescribed by $SST = 289$ K and $p_s = 1012.5$ hPa. Together with the initial profile for q_t this gives a relative humidity (RH) just above the surface of 85%. The RH just above the inversion is 38%.

Perturbed case

For the perturbed case the SST is increased to $SST = 291$ K and we keep a RH of 85% at the surface. That means that $q_{t,ml}$ is now increased by 1.326 g/kg to $q_{t,ml} = 10.926$ g/kg. We have kept the same inversion jump of specific humidity which means that q_{FA} also increases by 1.326 g/kg to $q_{FA} = 7.926$ g/kg. The RH just above the inversion increases then to 40%. We use the following initial profiles for the perturbed case:

$$\begin{aligned} 0 < z \leq 595 \text{ m} & \quad \begin{cases} \theta_l = 289.5 & (\text{K}) \\ q_t = 10.926 & (\text{g kg}^{-1}) \end{cases} \\ 595 < z \leq 1200 \text{ m} & \quad \begin{cases} \theta_l = 301.5 + 0.0075(z - 595) & (\text{K}) \\ q_t = 7.926 - 0.003(z - 595) & (\text{g kg}^{-1}) \end{cases} \end{aligned} \quad (4.2)$$

The geostrophic wind direction is $\alpha_{geo} = 305^\circ$ and the geostrophic wind speed is $U_{geo} = 6.0$ m s⁻¹, which results in the geostrophic forcing in the (x, y) direction:

$$(u, v) = U_{geo}(\cos \alpha_{geo}, \sin \alpha_{geo}). \quad (4.3)$$

Because the wind blows almost parallel to the isotherms of the sea surface temperature, the sea surface temperature hardly changes as the air flows south-eastwards so we may assume that the SST is constant. The surface roughness length is set to 2×10^{-4} m, and the Coriolis parameter at the prescribed latitude and longitude is $f_c = 8.0 \times 10^{-5}$ s⁻¹. The horizontal grid size is set to $\Delta x = \Delta y = 50$ meter. The vertical grid size is $\Delta z = 10$ meter.

4.1.2 Large scale forcings

For the large scale forcings we need to specify the subsidence rate \bar{w} and to balance the subsidence heating and drying, a large scale advection term has to be included in the simulation. The subsidence is given by

$$\bar{w} = -Dz \quad \text{for } 0 < z \leq 1200 \text{ m}, \quad (4.4)$$

where D is the divergence and is given by $D = 1 \times 10^{-5}$ s⁻¹. The large scale advection term is given by

$$0 < z \leq 1200 \text{ m} \quad \begin{cases} \left(\frac{d\theta_l}{dt}\right)_{LS} = -7.5 \times 10^{-8} \max(z, 500) & (\text{K s}^{-1}) \\ \left(\frac{dq_t}{dt}\right)_{LS} = 3.0 \times 10^{-11} \max(z, 500) & (\text{kg kg}^{-1} \text{s}^{-1}) \end{cases} \quad (4.5)$$

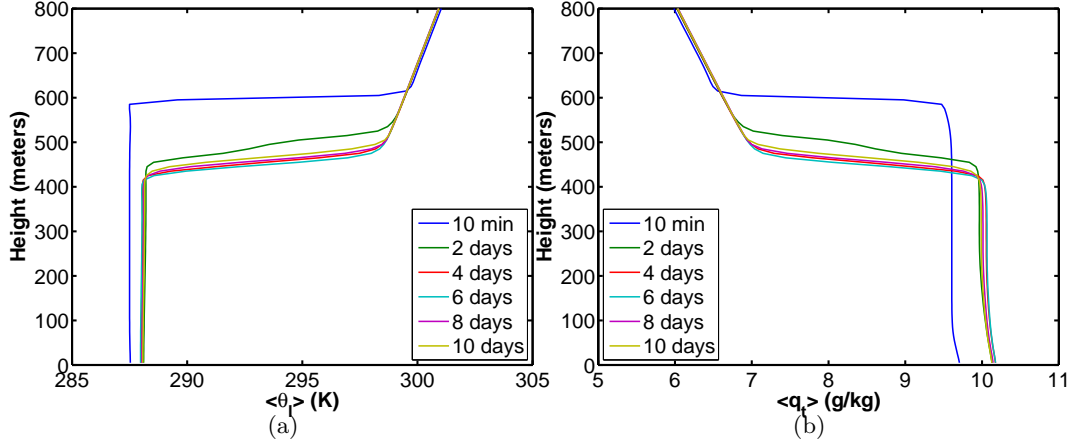


Figure 4.1: EUROCS case 1: the diurnally and horizontally averaged vertical profiles of a) θ_l and b) q_t for the period of 10 days.

These large scale advection terms have been chosen so that they approximately counteract the tendencies of the total specific humidity q_t and the liquid potential temperature θ_l .

The complete namoptions input file can be found in Appendix A.

4.2 Results

4.2.1 Case 1: $SST = 289$ K, diurnal radiation cycle

In Figure 4.1 the vertical profiles of θ_l and q_t are shown for the first case. It shows that the inversion height decreases until a height of around 450 meter. We can see that the diurnally averaged profiles of θ_l and q_t are fairly constant.

Figure 4.2 shows the diurnally averaged entrainment velocity versus the subsidence at z_i , the cloud fraction, and the LWP . We can see that the subsidence at z_i is higher than the entrainment rate for the first 4 days, causing the boundary layer top to sink. This is also being illustrated by Figure 4.2c. From this figure and Figure 4.2d we can also see a clear diurnal cycle in cloud depth. From Figure 4.2a we can see that this diurnal cycle in LWP goes along with a diurnal cycle in entrainment rate.

During daytime the cloud layer thins due to absorption of shortwave radiation and decoupling. The latter can be characterized by slightly negative buoyancy fluxes as can be seen from Figure 4.3a. This implies that moist thermals cannot reach the cloud layer, while entrainment maintains a steady supply of warm, dry air from above the inversion into the cloud layer. This results in a thinning of the cloud during daytime.

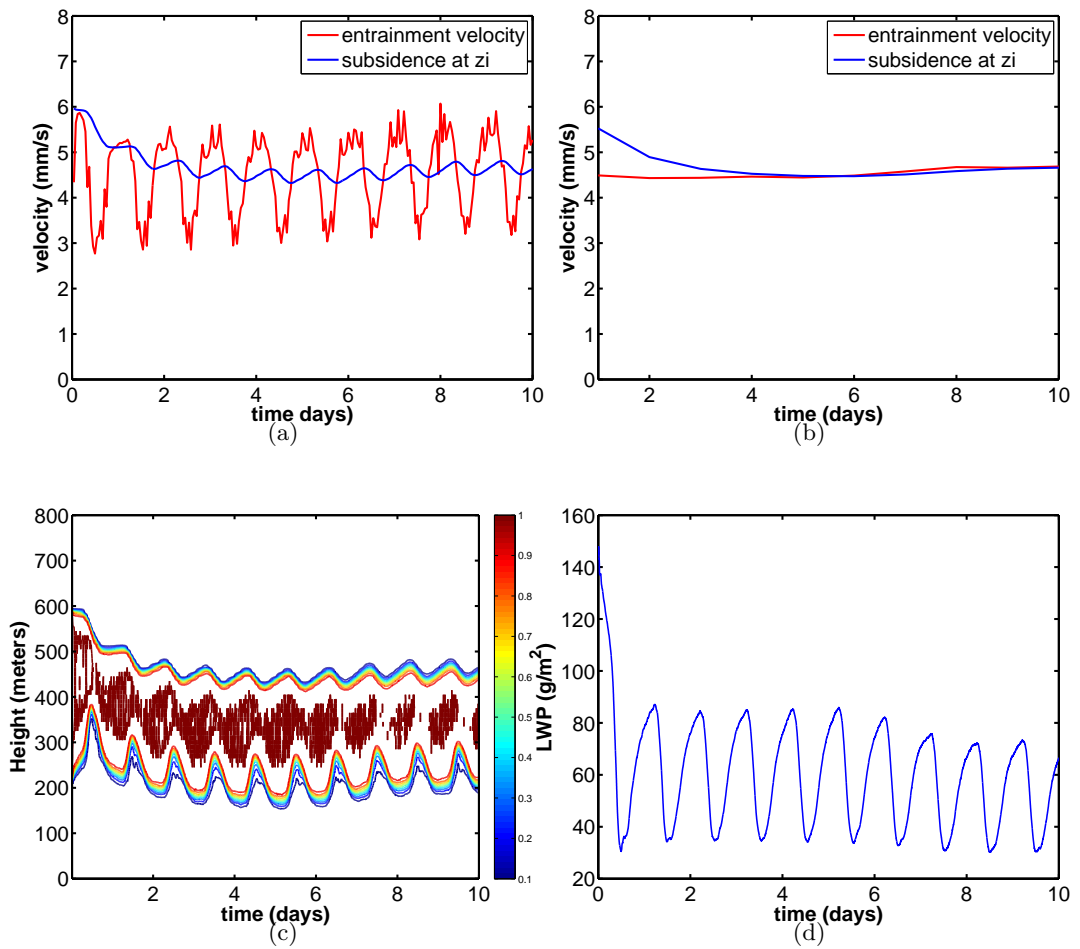


Figure 4.2: EUROCS case 1: The entrainment rate versus the subsidence at z_i for a) the hour mean and b) the diurnal mean. (c) is the cloud fraction and (d) the LWP for the period of 10 days.

We can compare these virtual potential temperature fluxes with the nighttime and daytime results from Duynkerke et al (2004), which are shown in Figure 4.3b and Figure 4.3c. We can see from Figure 4.3b that these profiles are roughly in agreement with the nighttime virtual potential temperature flux profile from GALEs. At daytime however it is notable that the virtual potential temperature flux profiles from GALEs are negative from the surface to the cloud base, while the buoyancy flux profiles in Figure 4.3c are not negative.

For further comparison between the GALES results and the LES results from Duynkerke et al (2004) we can zoom in on the graphs for the *LWP*, cloud fraction and entrainment, which is shown by Figure 4.4.

We can see from Figure 4.4a and Figure 4.4b that the *LWP* is quite low in GALES. From Figure 4.4c and Figure 4.4d we can see that the cloud top and cloud base are well within the limits of other LES models. If we compare Figure 4.4e to Figure 4.4f we see that the entrainment velocity is also lower than the LES mean, which could be a consequence of less radiative cooling at the cloud top due to a lower *LWP*. The entrainment rate is however within the limits of other LES.

It can be concluded that the *LWP* is in GALES lower than the 6 LES models for this case.

4.2.2 Case 2: $SST = 289$ K, constant diurnally averaged radiation

In the case we use a constant diurnally averaged radiative forcing it means that if we consider (3.15), we use a constant value $\cos(\beta) = 0.356$.

The vertical profiles of q_t and θ_l are similar in the case we use a constant diurnally averaged radiative forcing. Figure 4.5 shows the entrainment rate, cloud fraction and *LWP*. We can see now that the time series of hourly averaged entrainment rate, cloud fraction and *LWP* in Figure 4.5c and Figure 4.5d do not show a diurnal cycle anymore.

4.2.3 Comparison between case 1 and 2

In CGILS we use a constant radiative forcing to study equilibrium states. To determine the validity we compare the mean *LWP* over the last 2 days between case 1 where we use a diurnal cycle of the radiation and case 2 where we use a constant diurnally averaged radiation. The result can be seen in Table 4.1. It seems that the *LWP* decreases by 10 % if we use a

Case	$\langle LWP \rangle$ (g/m ²)	Relative difference
1	53.9	-
2	48.5	-10.0 %
Perturbed climate		
1	52.2	-
2	47.7	-8.6 %

Table 4.1: Average *LWP* values between the 8th and 10th day and the relative difference between case 1 and 2 in the current climate and in the perturbed climate.

constant diurnally averaged shortwave radiation.

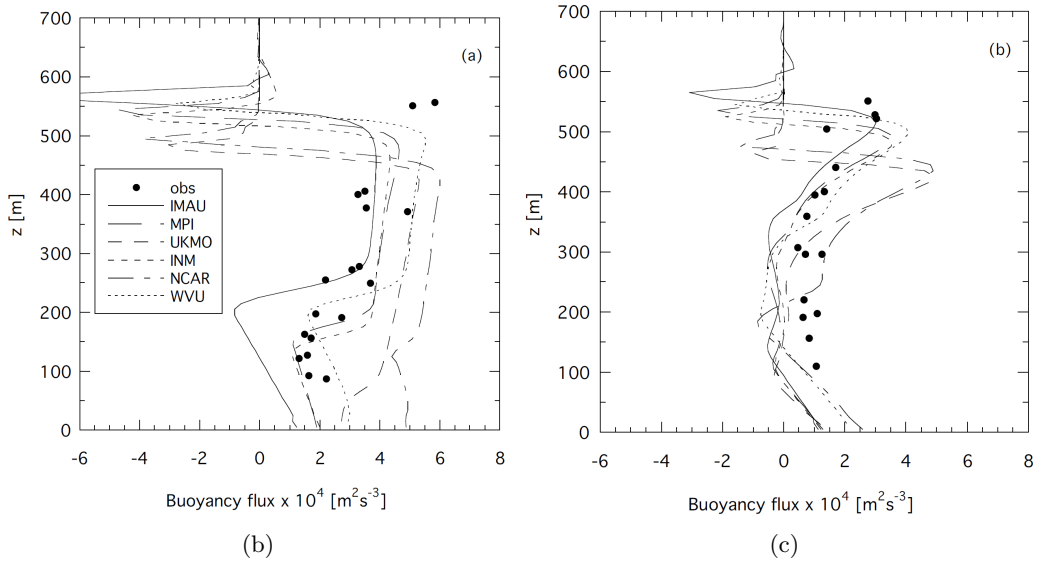
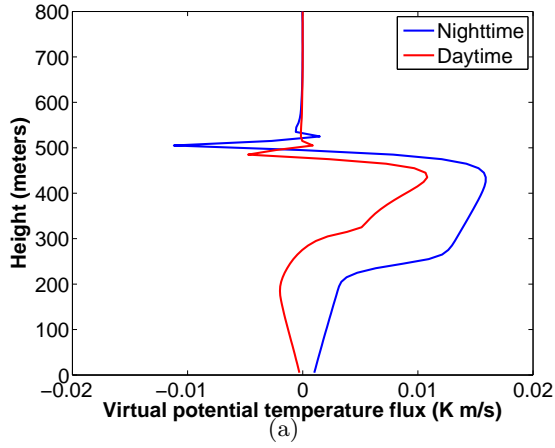


Figure 4.3: a) Virtual potential temperature flux profiles of GALEs during nighttime (averaged between 23 and 24 h) and daytime (averaged between 35 and 36 h local time). (b) and (c) are buoyancy flux profiles of 6 different LES models during nighttime (between 23 and 24 h) and daytime (between 35 and 36 h local time) respectively. During daytime decoupling is occurring due to negative buoyancy fluxes near the cloud base.

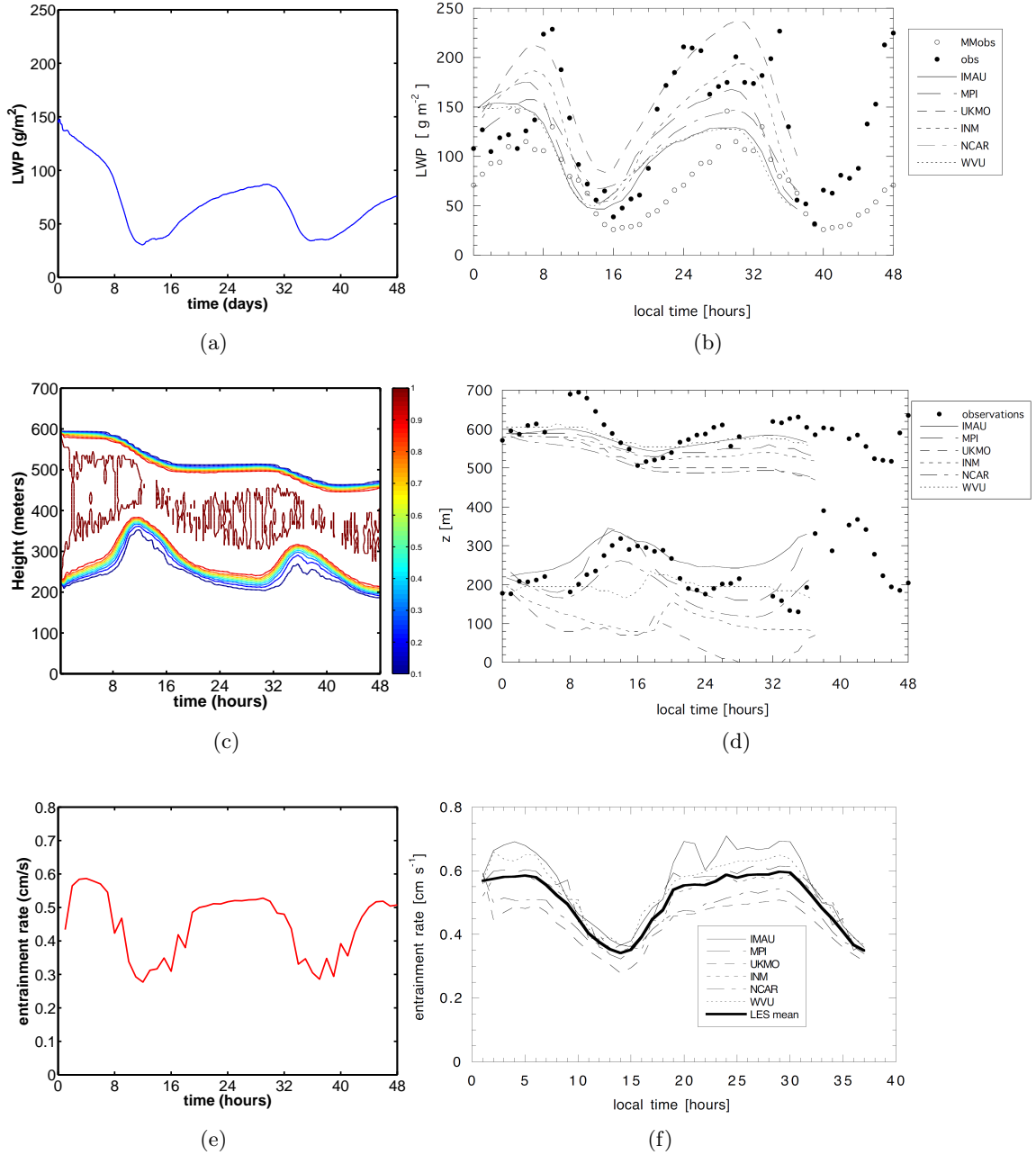


Figure 4.4: EUROCS case 1: A comparison of GALEs results on the left side with the results from 6 different LES models on the right side. (a) and (b) show the LWP , (c) shows the cloud fraction, (d) the cloud top and cloud base. (e) and (f) show the entrainment velocity.

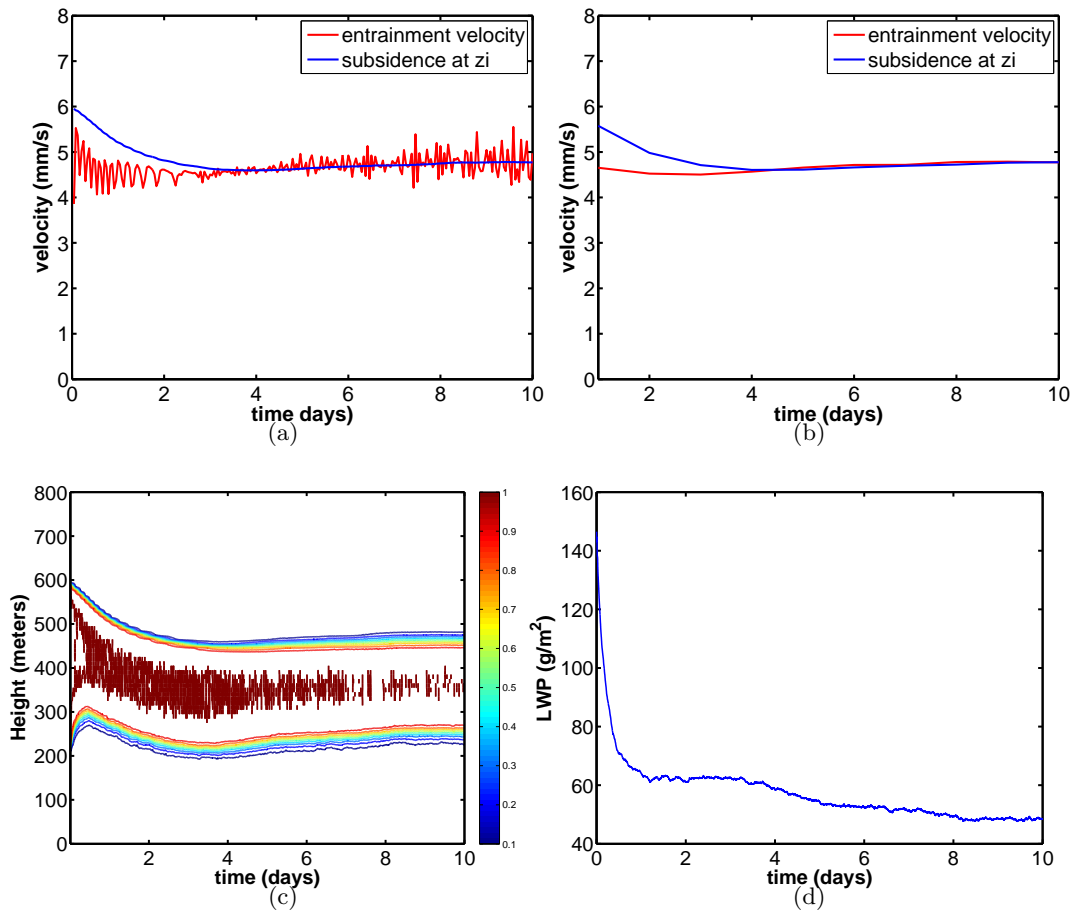


Figure 4.5: EUROCS case 2: time series of a) the hourly averaged entrainment rate versus the subsidence at z_i , b) the diurnally averaged entrainment rate versus the subsidence at z_i , c) the cloud fraction and d) the *LWP*.

In the perturbed climate the *SST* has been increased by 2 K to 291 K. There are similar profiles and time series as for the original cases. We can see from Table 4.1 that the *LWP* has decreased slightly and that the resulting *LWP* is again smaller if we use a constant diurnally averaged shortwave radiation. The relative difference is now 8.6%, which is slightly lower than for the original case.

From this it can be concluded that the *LWP* decreases by around 10% in the case that we use a constant diurnally averaged radiation which is moderate and that in a changing climate the significance even decreases. The use of a constant diurnally averaged radiation is therefore justified.

Chapter 5

CGILS: using GALEs to obtain steady-state solutions of the STBL

CGILS (CFMIP-GCSS Intercomparison of Large-Eddy and Single-Column Models) has been set-up to address the cloud-climate feedback in climate models by using Single-Column Models (SCM) and use LES to evaluate these SCM results. For further detail on this project see CGILS (2008). A Single Column Model is a physics package from a weather forecast or climate model and is used to calculate the evolution of the state of the atmosphere in one atmospheric column. It is in contrast to Large Eddy Simulation highly parametrized and one dimensional. They have the advantage that they require less computational power than LES and are therefore suitable tools to use in a large-scale model. The disadvantage is that they are less accurate than LES.

In this chapter we will use an idealized setting according to CGILS where we study STBL steady-state solutions of the phase space consisting of LTS and q_{FA} by using GALEs in order to quantify the effect on climate change. These results will then be compared with SCM results. Finally we will analyse the thermodynamic stability of the initial and final states to explain why some atmospheric conditions result in a clear ABL.

5.1 Case setup

In chapter 4 we have seen that the difference of a diurnal cycle of the solar radiation and a constant diurnally averaged solar radiation is approximately 10%. Because this difference is moderate, the simulations are performed with a constant incoming shortwave radiation at the top of the atmosphere as a diurnally averaged value of the specific latitude. The date, location and radiative forcing details are collected in Table 5.1.

Latitude (N)	32 °
Longitude (E)	129 °
Date	15 July 2003
ToA insolation (W/m^2)	471.5
$\Delta x, \Delta y$	50 m
L_x, L_y	6400 m
Δz	10 m
L_z	2500 m

Table 5.1: The date, location, radiative forcing at the top of the atmosphere, grid size and domain size.

Starting this research, the following boundary and initial conditions are applied:

1. the sea surface temperature (SST) is fixed.
2. the atmospheric temperature at the surface is 1.5 K colder than the SST.
3. the relative humidity, RH, at the surface is 80%.

The wind is set equal to the geostrophic wind in order to avoid oscillatory behaviour due to the Coriolis force:

$$U = 6.74 \text{ m/s} \quad (5.1)$$

The initial conditions are such that the ABL is vertically well mixed. That means that the conserved thermodynamic variables (θ_t and q_t) are constant with height up to a fixed ABL height (800 m).

We consider two sets of simulations:

1. The control (CTL) set: aimed to study the cloud thickness in the present climate;
2. P2K set: aimed to study the cloud feedback in a perturbed climate by looking at the *LWP* difference between the CTL set and the P2K set (where the SST has been increased by 2 K).

The thermodynamic variables are summarized in Table 5.2.

The large scale subsidence is chosen according to the approach used by Bellon and Stevens (2012):

$$\bar{w}(z) = -w_0(1 - e^{-\frac{z}{z_w}}), \quad (5.2)$$

where $w_0 = 3.5 \cdot 10^{-3}$ m/s and z_w is a scaling parameter and is set to $z_w = 500$ m.

	CTL set	P2K set
p_s (hPa)	1012.8	1012.8
SST (K)	292	294
θ_l (K)	289.5	291.5
q_t (g/kg)	9.7	11.
z_i (m)	800	800
u (m/s)	0	0
v (m/s)	-6.74	-6.74

Table 5.2: The parameters for the CTL set and the P2K set.

In order to use a realistic set-up we use in the free atmosphere a temperature lapse rate of

$$\frac{dT}{dz} = -6 \text{ K km}^{-1}. \quad (5.3)$$

Then the lapse rate of the potential temperature in the free atmosphere is approximately

$$\frac{d\theta}{dz} = 3.8 \text{ K km}^{-1}. \quad (5.4)$$

To reach a steady state, several variables need to be constant in time. This includes the potential temperature and the total specific humidity in the mixed layer and the free atmosphere (FA). The tendency of the temperature is given by (3.61b).

To determine the tendency due to radiation in the free atmosphere for the potential temperature, $\frac{\partial F}{\partial z}$ has to be determined. To this end, the radiation scheme of DALES (Heus et al, 2010) has been applied to the control case with an inversion jump of $\Delta\theta_l = 15 \text{ K}$ and $\Delta q_t = -4.5 \text{ g/kg}$. The radiation profiles resulting from these calculations are shown in Figure 5.1. As can be seen, the net radiation flux at the surface is much higher in the case that there is no cloud. From these radiation profiles $\frac{\partial F}{\partial z}$ for the free atmosphere can be determined. By using a linear fit as shown with the green dashed line in the figure this allows the use of a linear profile for the radiation, which is computationally cheaper. These fits are approximately identical for the two cases, therefore the same linear profile for the radiation is being chosen. In the case that there is a cloud, this source term is only being applied to the free atmosphere, that is, the region above the cloud top. But when there is no cloud, this cooling term is being applied to the whole vertical domain, including the mixed layer.

The linear fit of the radiation curves in Figure 5.1 gives

$$\frac{\partial F}{\partial z} \simeq 0.0132 \text{ W/m}^3. \quad (5.5)$$

When this radiative flux profile is being applied, it has been found that θ_l is not constant in time in the free atmosphere. That means that there is more cooling than subsidence warming. To keep the θ_l constant in the free atmosphere, the radiative cooling term needs to be lowered. We prefer to use a linear flux profile in accordance with the findings from the radiative transfer model of DALES. To obtain the required linear radiative flux profile for a steady-state free atmosphere, I used Matlab to model (3.61b). By trying several values, I found that there is a practically constant free atmosphere for

$$\frac{\partial F}{\partial z} = 0.0125 \text{ W/m}^3. \quad (5.6)$$

In steady-state this means that

$$\bar{w} \frac{\partial \theta}{\partial z} = -\frac{1}{\rho(z)c_p} \frac{\partial F}{\partial z}. \quad (5.7)$$

The tendency obtained using Matlab can be seen in Figure 5.2.

The resulting tendency GALEs gives is shown in Fig 5.3. As can be seen, θ_l is now practically constant.

5.1.1 GALEs

The namoptions of GALEs for the control case can be found in Appendix B. A run of 30 days with GALEs takes approximately 3 days of real time. To give an idea of the acceleration for this simulation by using a GPU instead of a CPU, we can compare the time it takes for running this simulation with GALEs to the time it takes for a similar run with DALES. A similar run of 30 days with DALES on a node of 32 processors on supercomputer HUYGENS, takes approximately 13 days of real time, which is ~ 10000 hours or 417 days using only one processor. This would be a very expensive simulation. If we compare this run on DALES with one processor to this run on GALEs with one GPU, the acceleration factor would be around 140. It should be noted however that GALEs does not use the full radiation scheme (Rapid Radiative Transfer Model) which is computationally very expensive.

5.2 Results

5.2.1 Control case

Figure 5.4a to Fig 5.4f show for the control case where $\Delta\theta_l = 15 \text{ K}$ the evolution of the θ_l , q_t profiles and the time series of w_e plotted versus the subsidence \bar{w} at z_i , the cloud fraction (which is at a certain height the fraction of the domain size in which liquid water is present), the *LWP* and the buoyancy flux profile. From Figure 5.4a it can be seen that the

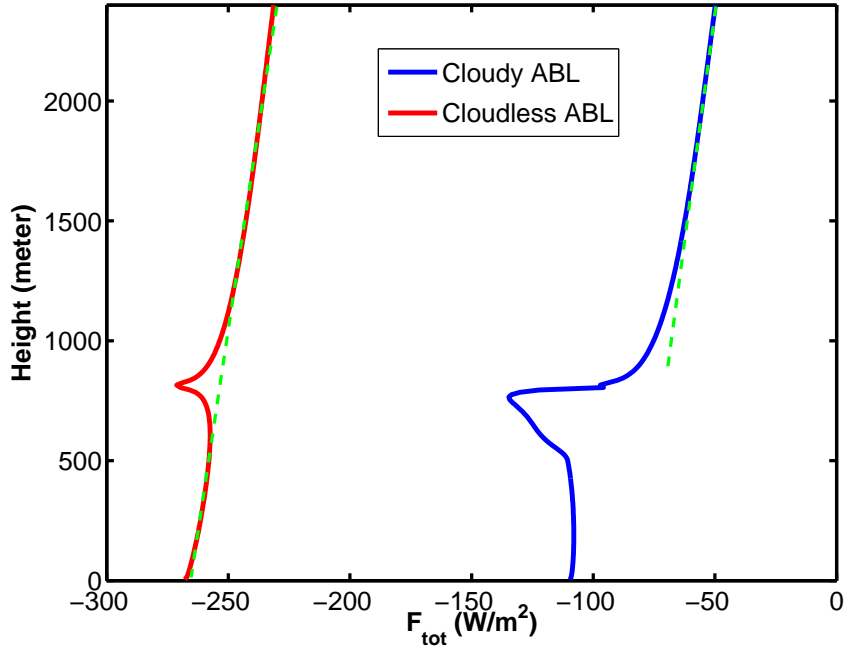


Figure 5.1: The SW+LW radiation profiles for the case where there is a Sc cloud and for the case where there is no cloud in the atmosphere. Here the x-axis represents the total radiation F , while the y-axis represents the height z . The green dashed line represents a linear fit to determine $\frac{\partial F}{\partial z}$.

liquid water potential temperature has reached a steady-state. It can also be observed that z_i stays constant after around 20 days, while the LWP stays also constant. From the q_t profile in Figure 5.4b we can see that there is a gradient of the specific humidity in the mixed layer. This means that it is not well mixed and that there is some decoupling occurring. This is being supported by Figure 5.4f where it can be seen that there are slightly negative buoyancy fluxes near the cloud base. If there are only small negative buoyancy fluxes, moist thermals can still reach the cloud base, but they cannot when these negative buoyancy fluxes are sufficiently high. This has the consequence that the cloud separates into two cloud layers. Note that a negative surface buoyancy flux which can be seen from Figure 5.4f also shows a stable stratification. The sea surface now cools the ABL instead of heating it and together with the longwave radiative cooling at the cloud top this compensates the warming of the ABL due to entrainment, which leads to a steady-state liquid water potential temperature in the ABL.

In the case that $\frac{\partial q_t}{\partial z} \neq 0$ (and no precipitation) we know from (2.42) that

$$\frac{\partial q_t}{\partial t} = -\frac{\partial \overline{w'q_t'}}{\partial z} - \overline{w} \frac{\partial q_t}{\partial z}. \quad (5.8)$$

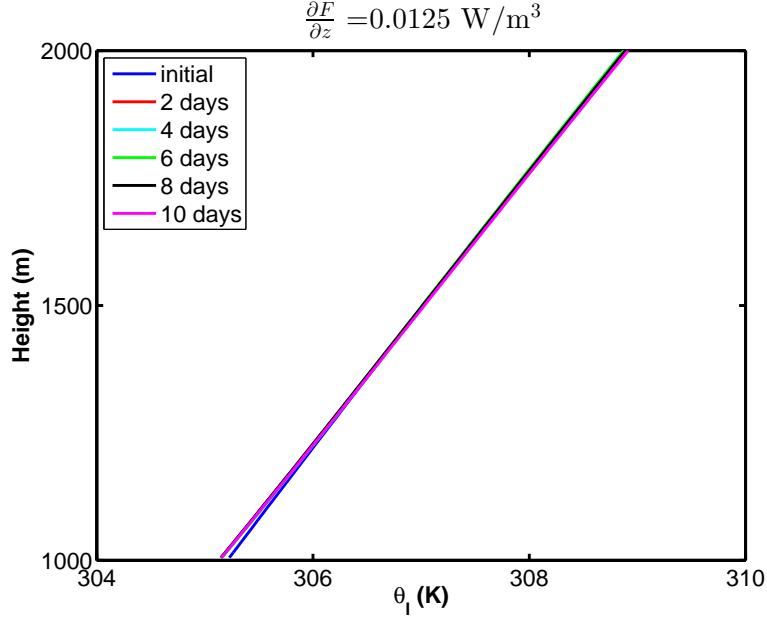


Figure 5.2: The vertical profiles of θ_l in the free atmosphere modelled using Matlab for $\frac{\partial F}{\partial z} = 0.0125 \text{ W/m}^3$. It shows that there is no tendency in θ_l .

In a steady-state, $\frac{\partial q_t}{\partial t}$ needs to be zero. Figure 5.5a and 5.5b show the vertical gradient of the specific humidity turbulent flux $-\overline{w'q_t'}$ and $-\overline{w} \frac{dq_t}{dz}$ respectively. The sum of these contributions is the tendency of q_t in the ABL and is shown by Figure 5.5c. It can be seen that this tendency is approximately zero.

From a steady-state temperature, specific humidity and z_i it can be concluded that this Sc cloud is in equilibrium. Next we can determine the averaged steady-state values of the LWP , w_e , z_i and z_b .

The next step is to vary the initial inversion jump of θ_l ($\Delta\theta_l$) in steps of 2 K in the interval where $\Delta\theta_l \in [9, 17]$ K. For plotting purposes these inversion jumps will be converted to the Low Tropospheric Stability (LTS), which is defined as

$$\begin{aligned} LTS &= \theta_l|_{z=3000\text{m}} - \theta_{l,0} \\ &= \theta_{ref} + \Gamma_{\theta} z_{LTS} - \theta_{l,0}, \end{aligned} \quad (5.9)$$

with $z_{LTS} = 3000 \text{ m}$.

Secondly we change the specific humidity inversion jump to $\Delta q_t = -2.5 \text{ g/kg}$ and $\Delta q_t = -6.5 \text{ g/kg}$, which corresponds to $q_{FA} = 7.2 \text{ g/kg}$ and $q_{FA} = 3.2 \text{ g/kg}$. In this way we cover a part of the phase space consisting of the inversion jumps of LTS and specific humidity. In the next step we

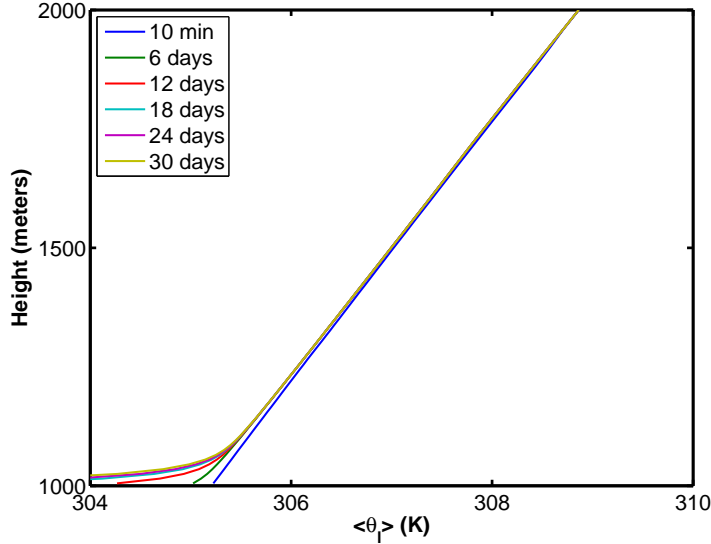


Figure 5.3: The vertical profiles of θ_l in the free atmosphere for a 30-day simulation of the control case by using GALEs. It shows that there is also no tendency in the FA using GALEs.

perturb in the context of climate change the SST with 2 K to $SST = 294$ K and we use the same set of LTS and specific humidity inversion jumps.

5.2.2 Control set

The results of the first set of temperature inversion jumps $\Delta\theta_l$ are tabulated in Table 5.3. We can see that a lower LTS results in a higher inversion height z_i . This is in accordance with (3.45). When the inversion jump of temperature decreases, it is easier to entrain air from just above the inversion layer into the cloud. It can also be seen that a smaller LTS results in a higher LWP , which is related to the fact that the difference between z_i and the cloud base z_b increases. Figure 5.6 shows the profiles and the evolution of the thermodynamic variables for experiment 4 with the $LTS = 17.7$ K. We can see that the inversion height is clearly higher than for the control case and we can also see from Figure 5.6a and 5.6b that the ABL has been decoupled into two separate layers. The lower layer has a much higher total water content and a slightly lower θ_l than the upper layer. Despite the high specific humidity in the lower layer, the temperature is sufficiently high for the air to remain unsaturated. The upper layer has a much lower specific humidity which has the consequence that the air becomes saturated at a

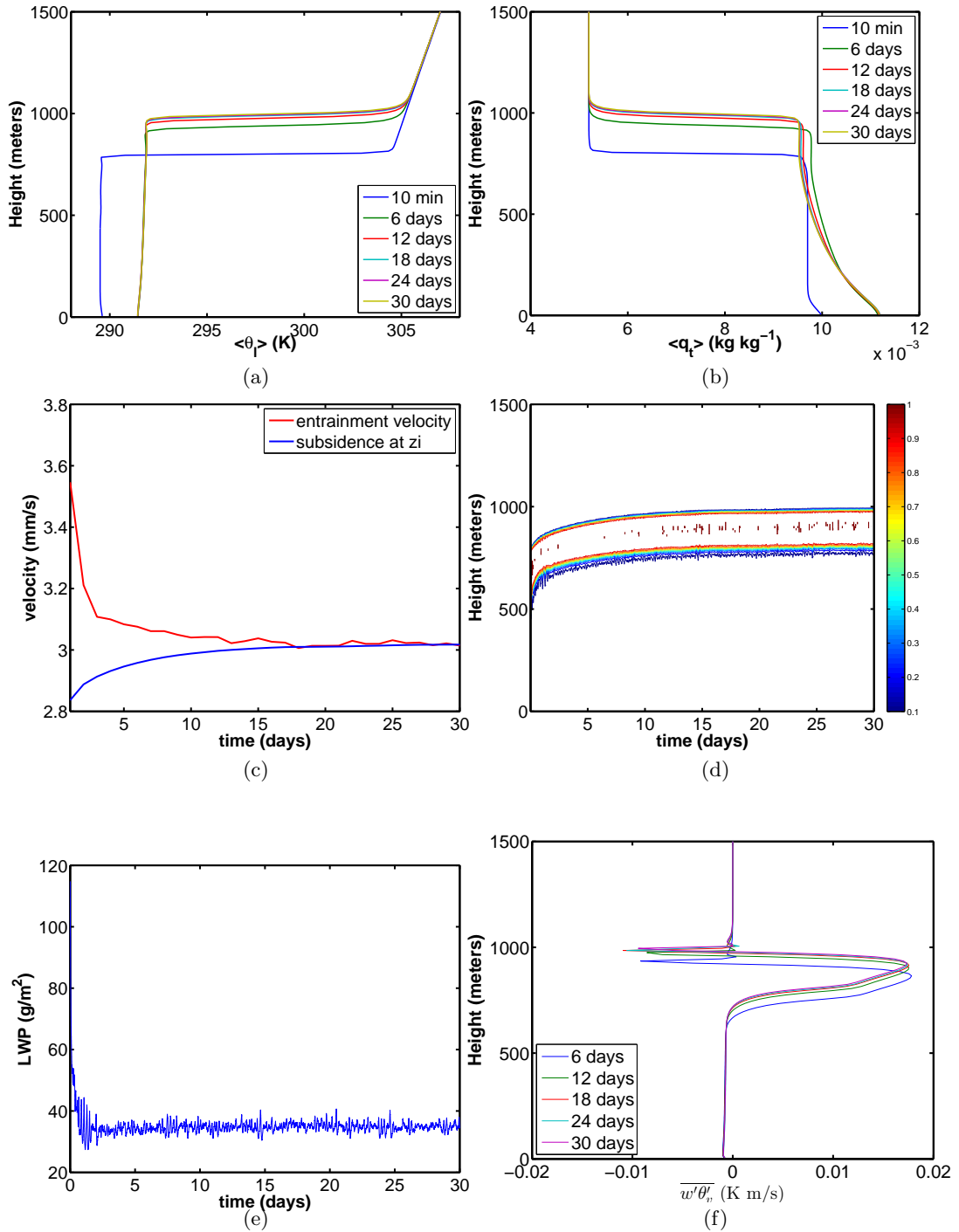


Figure 5.4: Control case: The diurnally averaged vertical profiles for different times of a) θ_t and b) q_t . (c) is the entrainment velocity plotted together with the subsidence at z_i , (d) the cloud fraction, (e) the LWP and (f) the $\overline{w'\theta'_v}$ profile. All of these are also horizontal averages.

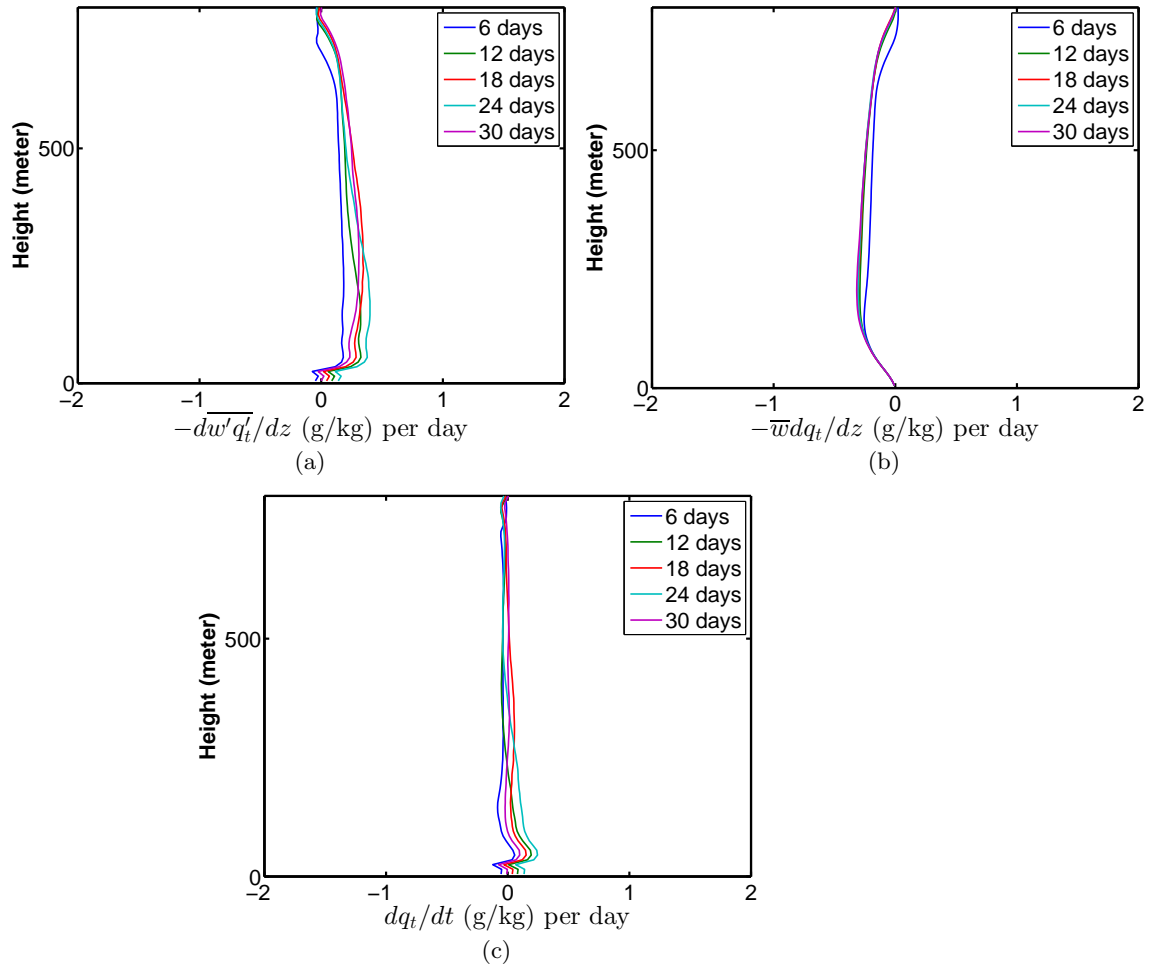


Figure 5.5: Control case: diurnally averaged a) vertical specific humidity flux gradient, b) subsidence drying and c) the q_t tendency in the mixed layer for different times.

Expnr	1	2	3	4	5	
LTS	23.9	21.8	19.8	17.7	15.7	K
$\Delta\theta_l _{t=0}$	17	15	13	11	9	K
$\Delta q_t _{t=0}$	-4.5	-4.5	-4.5	-4.5	-4.5	g/kg
q_{FA}	5.2	5.2	5.2	5.2	5.2	g/kg
$\Delta\theta_l _{t_{\text{end}}}$	13.4	12.4	11.9	10.0	3.3	K
$\Delta q_t _{t_{\text{end}}}$	-5.2	-4.3	-2.8	-2.1	-5.8	g/kg
LWP	34.4	35.9	38.6	48.4	0	g/m ²
w_e	2.74	3.01	3.26	3.37	0.91	mm/s
z_i	777	982.4	1351	1572	148	m
z_b	593	792	1141	1340	-	m

Table 5.3: Steady-state results of inversion jumps of temperature and specific humidity, the Liquid Water Path, entrainment velocity, ABL height and cloud base for a range of inversion jumps averaged over the 30th day.

quite high altitude: 1340 m. Compared to a vertically well mixed layer we have a thinner cloud.

Despite this effect, the cloud thickness is still higher than in the control case, as we can see if we compare Figure 5.6e with Figure 5.4e. This is a result of a much higher z_i .

In experiment 5 with the $LTS = 15.7$ K, we see that after a spin-off period of ± 1 day the Sc cloud rapidly dissipates. This is illustrated by Figure 5.7. Figure 5.7f shows large negative buoyancy fluxes near the cloud base which causes decoupling and together with a high entrainment rate this causes the Sc to dissolve. The next thing that happens is that the entrainment rate diminishes, due to the absence of longwave radiative cooling of the cloud, and the ABL collapses to a low ABL height.

In Table 5.4 the steady-state results are shown for the case where the $LTS = 19.8$ K and where the inversion jump of specific humidity has been increased or decreased with 2 g/kg. It can be seen that a lower Δq_t leads to a higher LWP but lower z_i . This can be explained by considering that a smaller Δq_t means less drying of the ABL. The inversion height is lower because less drying means less evaporative cooling which is a driving mechanism for the entrainment rate. According to (3.30) a lower entrainment rate results in steady-state in a lower z_i .

We can see that in experiment 8 with $q_{FA} = 3.2$ g/kg the cloud completely disappears. This is similar to experiment 5 with the $LTS = 15.7$ K, which is illustrated by Figure 5.7. Apparently the enhanced drying is too much to maintain a cloud. The absence of a cloud results in much less radiative cooling and consequently a much lower entrainment rate. The ABL shrinks to $z_i = 107$ m. A reason why the inversion does not decay to zero could be because now the radiative cooling that was used only in the free

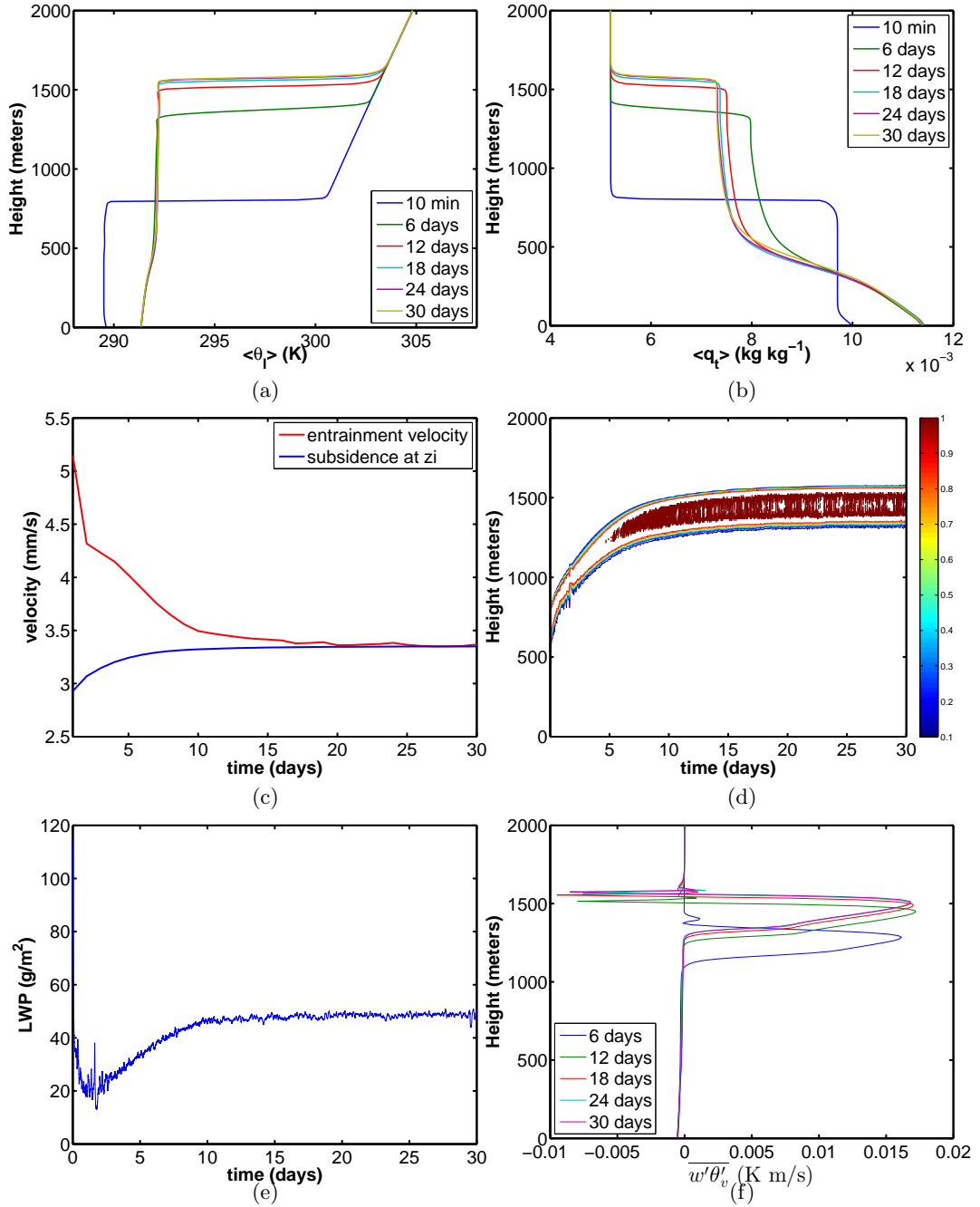


Figure 5.6: Experiment 4 with $LTS = 17.7$ K ($\Delta\theta_l|_{t=0} = 11$ K): The diurnally averaged vertical profiles for different times of a) θ_l and b) q_t . (c) is the entrainment velocity plotted together with the subsidence at z_i , (d) the cloud fraction, (e) the LWP and (f) the $\overline{w'\theta'_v}$ profile. All of these are also horizontal averages.

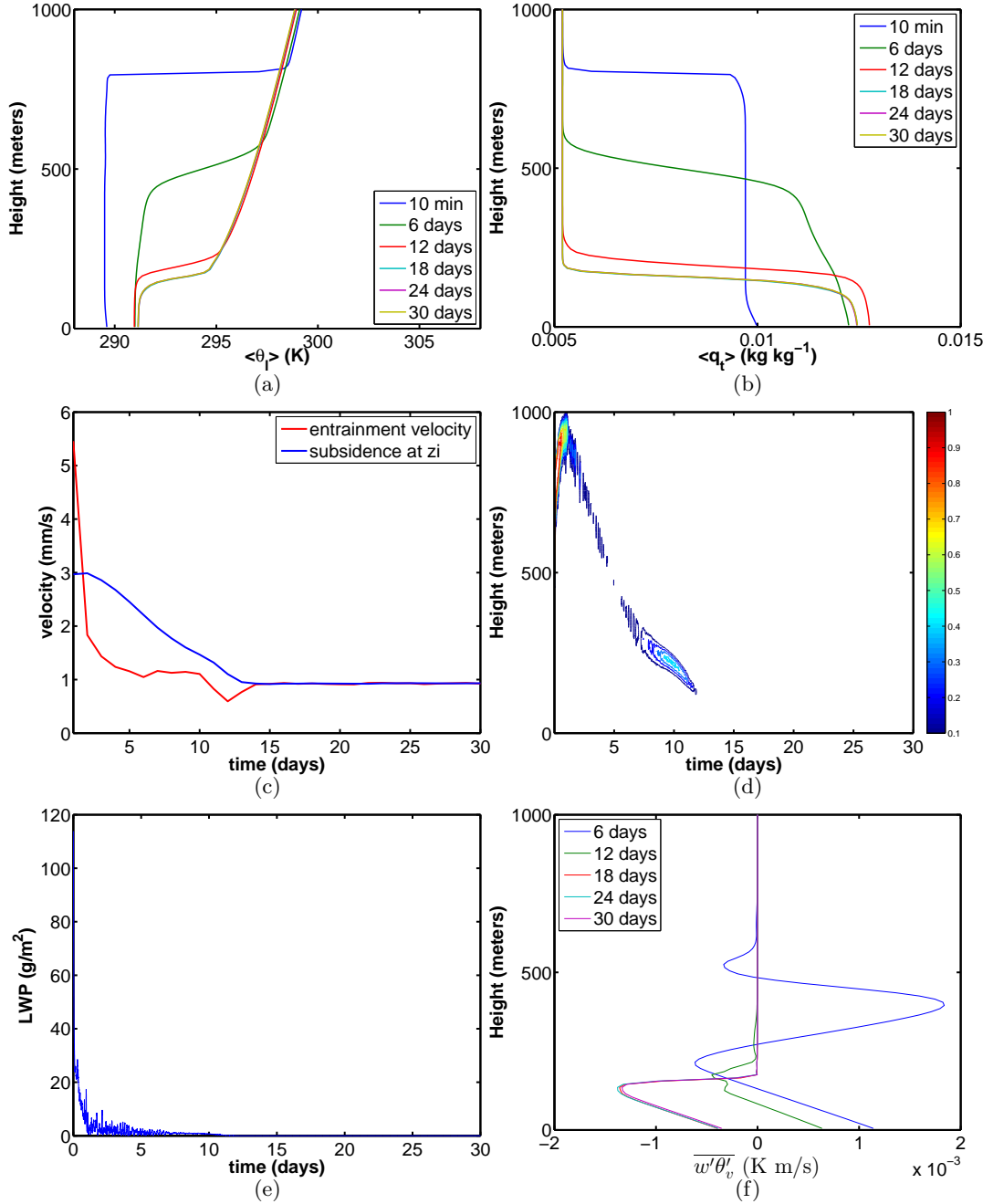


Figure 5.7: Experiment 5 with $LTS = 15.7$ K ($\Delta\theta_l|_{t=0}$): The diurnally averaged vertical profiles for different times of a) θ_l and b) q_l . (c) is the entrainment velocity plotted together with the subsidence at z_i , (d) the cloud fraction, (e) the LWP and (f) the $\overline{w'\theta'_v}$ profile. All of these are also horizontal averages. It can be observed that the cloud rapidly dissipates.

Expnr	6	7	8	
LTS	19.8	19.8	19.8	K
$\Delta\theta_l _{t=0}$	13	13	13	K
$\Delta q_t _{t=0}$	-2.5	-4.5	-6.5	g/kg
q_{FA}	7.2	5.2	3.2	g/kg
$\Delta\theta_l _{t_{\text{end}}}$	12.0	11.9	5.9	K
$\Delta q_t _{t_{\text{end}}}$	-1.5	-2.8	-8.8	g/kg
LWP	40.8	38.6	0	g/m ²
w_e	3.17	3.26	0.68	mm/s
z_i	1202	1351	107	m
z_b	990	1141	-	m

Table 5.4: Steady-state results of inversion jumps of temperature and specific humidity, the Liquid Water Path, entrainment velocity, ABL height and cloud base averaged over the 30th day.

atmosphere for a STBL, is now extended to the whole layer including the CBL. Another effect is that in GALES, TKE due to wind shear is responsible for some entrainment. The quantity of this effect will however not be investigated in this study.

5.2.3 P2K set

In the perturbed case we increase the SST by 2 K, $q_{t,ml}$ increases from 9.7 g/kg to 11 g/kg to keep the same relative humidity at the lowest level in the atmosphere. To keep the same inversion jump of specific humidity q_{FA} also increases with 1.3 g/kg. In the unperturbed case the RH just above the inversion was 24.1%. In the perturbed case the RH just above the inversion is increased by 2.5% to 26.6%.

We repeat the same set of simulations. The results are shown in Table 5.5. If we compare these results with the unperturbed results in Table 5.3 we can see that the LWP has been decreased by 29% for the $LTS = 23.9$ K. z_i has increased by $\Delta z_i = 14$ m while $\Delta z_b = 36$ m. For the case of $LTS = 21.8$ K we see also a decrease of LWP , in this case around 24%. This is a clear **positive feedback**. We can also see from the thermodynamic profiles that there is a vertical gradient in the temperature and specific humidity profiles in the ABL. This, together with negative buoyancy fluxes under the cloud layer indicate decoupling. A higher SST results in a deeper ABL which generally results in a higher degree of decoupling (Wood and Bretherton, 2004).

For the case of $LTS = 19.8$ K and where we vary Δq_t with 2.5 g/kg we see also a (slight) decrease in LWP , and z_i and z_b have increased compared to the current climate. For $LTS = 17.7$ K however, we see a slight increase

expnr	9	10	11	12	13	
LTS	23.9	21.8	19.8	17.7	15.7	K
$\Delta\theta_l _{t=0}$	17	15	13	11	9	K
$\Delta q_t _{t=0}$	-4.5	-4.5	-4.5	-4.5	-4.5	g/kg
q_{FA}	6.5	6.5	6.5	6.5	6.5	g/kg
$\Delta\theta_l _{t_{\text{end}}}$	14.6	13.5	12.1	10.3	2.7	K
$\Delta q_t _{t_{\text{end}}}$	-4.5	-4	-2.7	-1.6	-5.1	g/kg
LWP	24.4	27.3	38.3	49.2	0	g/m ²
ΔLWP	-10.0	-8.6	-0.3	0.8	0	g/m ²
w_e	2.78	3.09	3.27	3.38	0.93	mm/s
z_i	791	1056	1356	1591	154	m
z_b	629	881	1152	1360	-	m

Table 5.5: Steady-state results of inversion jumps of temperature and specific humidity, the Liquid Water Path, entrainment velocity, ABL height and cloud base averaged over the 30th day for the perturbed case where $SST = 294$ K. $\Delta q_t = -4.5$ g/kg is kept constant which translates to $q_{FA} = 6.5$ g/kg.

in LWP and again a higher z_i and z_b . But we can see that in general Sc give with a SST increase a positive feedback. If $\Delta q_t = -6.5$ g/kg we see again that the cloud disappears for long times.

5.2.4 Comparison with the Single Column Model Ec-Earth

We can use the LES results to evaluate the results from the SCM Ec-Earth. These SCM results are obtained by using the *cycle 31r1 plus dual mass flux* scheme for convection, and using identical forcing conditions. The results are shown in Figure 5.8.

If we compare Figure 5.8a with the results of Table 5.3, we see that for high LTS the LWP values of the SCM are much higher than the LES results. Only the result of $LTS = 17.7$ K is similar to the SCM value. We see also the opposite trend in Figure 5.8a: when the LTS decreases we see a decrease in LWP , while the LES results from Table 5.3 clearly show an increase in LWP when the LTS decreases. Only when the $LTS = 15.7$ K we see a collapse of the LWP in the LES results.

Figure 5.8b shows the cloud top height which is co-located to z_i . We can see that for $LTS = 23.9$ K the resulting inversion height z_i is approximately the same. If we compare the inversion height results of the lower LTS values of Table 5.3 with the SCM results, we see that the LES results are higher: $LTS = 19.8$ K gives $z_i = 1351$ m while the SCM gives $z_i \simeq 1000$ m.

From Figure 5.8c we can see that z_b is significantly lower than the LES results. z_b also does not seem to increase much when the LTS decreases

expr	14	15	16	
LTS	19.8	19.8	19.8	K
$\Delta\theta_l _{t=0}$	13	13	13	K
$\Delta q_t _{t=0}$	-2.5	-4.5	-6.5	g/kg
q_{FA}	8.5	6.5	4.5	g/kg
$\Delta\theta_l _{t_{end}}$	11.8	12.1	5.2	K
$\Delta q_t _{t_{end}}$	-1.2	-2.7	-7.4	g/kg
LWP	40.0	38.3	0	g/m ²
ΔLWP	-0.8	-0.3	0	g/m ²
w_e	3.17	3.27	0.68	mm/s
z_i	1272	1356	107	m
z_b	1063	1152	-	m

Table 5.6: Steady-state results of inversion jumps of temperature and specific humidity, the Liquid Water Path, entrainment velocity, ABL height and cloud base averaged over the 30th day for $SST = 294$ K.

which is not in accordance with the results in Table 5.3.

Figure 5.8d shows a negative feedback in a changing climate for the right part of the phase space, which is not in agreement with the LES results where we found a clear positive feedback.

In general we can see that there is no agreement between the LES and the SCM results.

5.2.5 Thermodynamic stability analysis

By using the CTEI criterion, which has been introduced by (3.51) in section 3.2.3, we can analyse the thermodynamic stability of the GALES results and in this way we can explain why a STBL transitions under certain atmospheric conditions (low LTS , low q_{FA}) to a clear ABL and remains cloudy under other conditions (high LTS , high q_{FA}). These GALES results can be translated to the phase space consisting of the inversion jumps of temperature and specific humidity, as shown in Figure 5.9.

In this figure, the skew dashed line represents the boundary between unstable (positive buoyancy flux at cloud top, CTEI) and stable solutions (negative buoyancy flux at cloud top).

We can identify three groups from this figure. In every group we see that compared to the initial state the temperature jump at the inversion decreases for the final state. This can be explained by the effect of an increase of temperature in the ABL, which is higher than the increase of temperature jump at the inversion due to a higher ABL and higher FA temperature at the inversion.

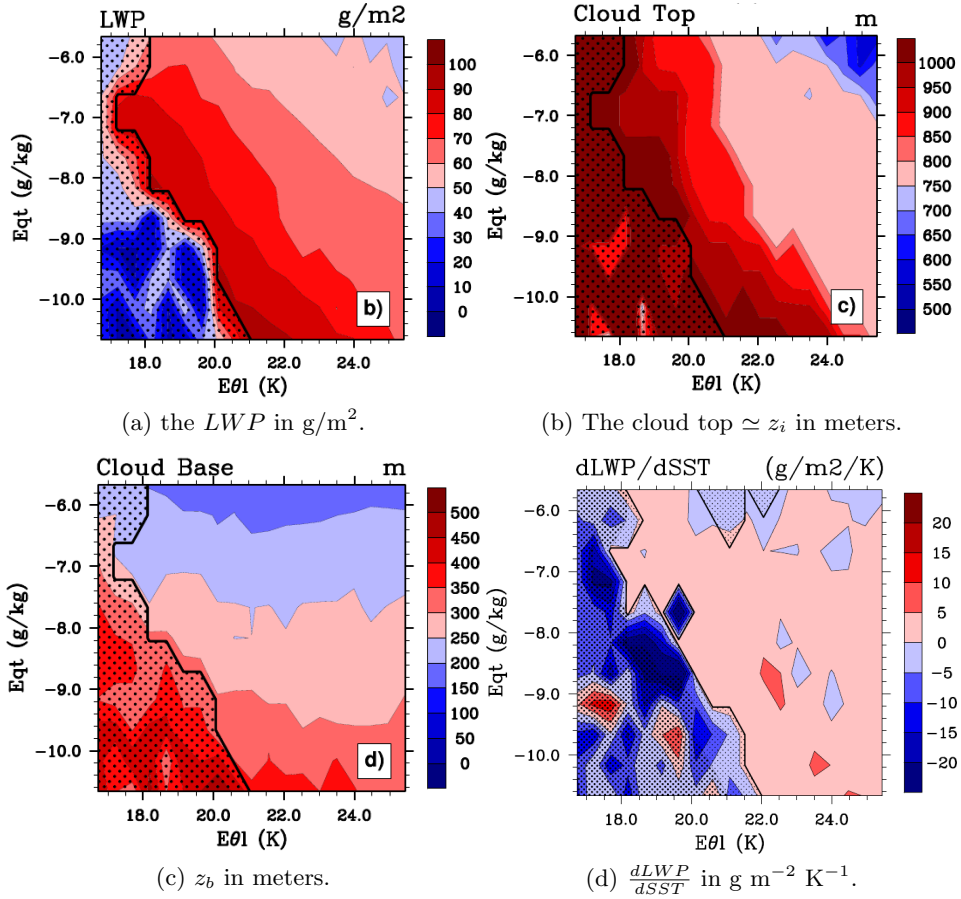


Figure 5.8: SCM Ec-Earth results for the cloud top, cloud base, LWP and $dLWP/dSST$. $Eq_t = q_{t,fa} - q_{t,0}$ and $E\theta_1 = LTS$. $q_{t,fa} - q_{t,0} = -8.16 \text{ g/kg}$ for the LES CTL set where $\Delta q_t = -4.5 \text{ g/kg}$. The gray area shows the region where $\frac{\sqrt{\langle x^2 \rangle}}{\langle x \rangle} \geq 30\%$, which indicates a high variation of x around the mean value.

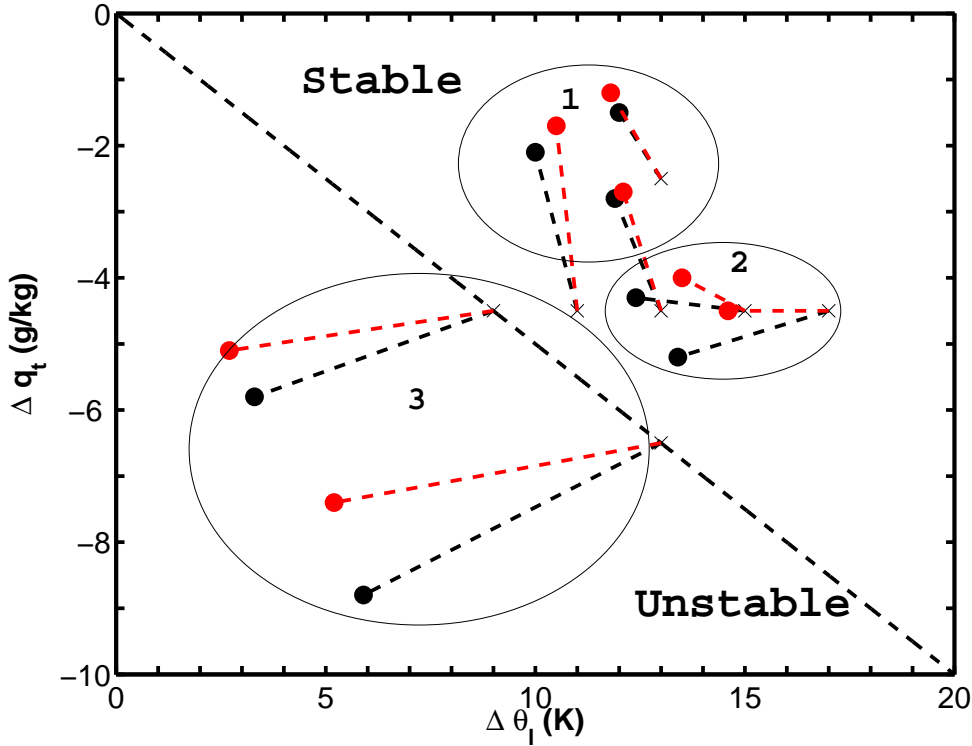


Figure 5.9: The $(\Delta\theta_l, \Delta q_t)$ plane showing the thermodynamic instability curve and the LES results including the "current" climate (black dots and lines) and perturbed climate (red dots and lines). The crosses represent the initial states and the filled dots represent the steady-state solutions. The left portion of the figure shows unstable states which corresponds to experiment 5, 8, 13 and 16, and result in a clear ABL. The right portion shows stable states corresponding to the other experiments which result in a cloudy ABL.

In group 1 we see that the final state consists of a much smaller inversion jump of specific humidity. This can be characterized by experiment 4 in Figure 5.6b where we see that in steady-state the ABL is very deep and that there is a high degree of decoupling. The specific humidity jump at the inversion is much smaller than in the initial state.

In the perturbed case we see transitions to slightly smaller inversion jumps of specific humidity, which could indicate a slightly higher degree of decoupling as the difference between the specific humidity close to the surface and the specific humidity close to the inversion increases.

Group 2 tends to move to a different region. We can see a smaller change in the inversion jump of specific humidity than for group 1. It can be characterized by the control case, which is experiment 2 and shown in Figure 5.4, where it can be seen that the inversion jump of specific humidity indeed hardly changes, while the inversion jump of temperature decreases.

In the P2K case we see that these inversion jumps of specific humidity also decrease.

Group 3 includes initial states right at the CTEI curve. We can see that the final state is clearly in the unstable region. This group can be characterized by experiment 5 in Figure 5.7. We can see that after a spin-off period of

± 1 day the Sc cloud rapidly dissipates. Figure 5.7f shows large negative buoyancy fluxes near the cloud base which causes decoupling and together with a high entrainment rate this causes the Sc to dissolve. The next thing that happens is that the entrainment rate diminishes, due to the absence of longwave radiative cooling of the cloud, and the ABL collapses to a low ABL height.

The perturbed case shows again a decrease in the inversion jump of specific humidity.

It can be concluded that states in the unstable region of the phase space indeed correspond to a final state that is a clear ABL, while states in the stable region correspond to a final state that is a cloudy ABL.

Chapter 6

Mixed-Layer Model: equilibrium states of an initially clear/cloudy ABL

To gain more insight in equilibrium states and cloud amount of Sc, we can use the MLM to study equilibrium solutions of clear and cloudy ABLs. It will be shown here that if we consider the phase space consisting of the inversion jumps of specific humidity and LTS there are parts where an initially clear ABL remains clear and that there are also areas where the final state is a clear stable ABL or a cloudy ABL.

Using the entrainment parametrization of Moeng, it will be shown that an initially cloudy ABL will always remain cloudy.

The effect of some important processes like radiative cooling, windspeed and a changing climate will also be elaborated on in this chapter using this model. First of all I will give a detailed explanation of the theory and secondly I discuss the numerical results.

6.1 Case setup

For this case we use again a large scale subsidence which is an exponential function depending on z given by (5.2).

The specific humidity in the free atmosphere $q_{t,fa}$ is taken as a constant value with time and height. The potential temperature of the free atmosphere is given by (3.40).

For the calculation of F' we use a constant density $\rho_0 = 1.14 \text{ kg/m}^3$. We vary the LTS ($LTS \in [18, 24] \text{ K}$) and $(q_{t,fa} - q_{t,0})$ ($(q_{t,fa} - q_{t,0}) \in [-0.010, -0.002] \text{ kgkg}^{-1}$).

In summary we have the following values for the set of parameters used

Parameter	Value
A_{θ_v}	0.2
Γ_θ (K/m)	$6 \cdot 10^{-3}$
C_D	0.001
b_m (m ² /kg)	0.9
ρ_0 (kg/m ³)	1.14
C_{rad} (K/s)	$2/(24 \cdot 3600)$
κ (m ² /s)	130
w_0 (m/s)	$3.5 \cdot 10^{-3}$
z_w (m)	500
dF_L (W/m ²)	40
F' (K m/s)	0.035
p_s (hPa)	1012.8
$A_{1,max}$	1
LTS (K)	[18, 24]
$q_{t,fa} - q_{t,0}$ (kgkg ⁻¹)	[-0.010, -0.002]

Table 6.1: The values of the parameters used in equations (6.5) and (6.10) for all the experiments.

Experiment	U (m/s)	SST (K)
1	3	292
2	6.74	292
3	6.74	294

Table 6.2: The values of the variables used in the different experiments

in (6.5) and (6.10), which can be seen in Table 6.1. We conduct three experiments to study the effect of windspeed and SST on the steady-state solutions. The values of the changing variables can be seen in Table 6.2.

6.1.1 Steady-state analytic solutions for an initially clear ABL

From (3.29) and (3.38) we know that

$$w_e \Delta \theta_v = A_{\theta_v} \overline{w' \theta'_v}|_0. \quad (6.1)$$

In an equilibrium state the entrainment velocity is equal to the subsidence at the mixed-layer top. That means we have (using (3.40), (3.41) and (6.1)):

$$w_e = w_0 (1 - e^{-z_i/z_w}) = \frac{A_{\theta_v} C_D |\vec{U}| (\theta_{v,0} - \theta_{v,ml})}{(\theta_{ref} + \Gamma_\theta z_i)(1 + \epsilon_I q_{t,fa}) - \theta_{v,ml}} \quad (6.2)$$

Equation (3.52) dictates that in a steady-state, the radiative cooling must balance the warming due to turbulence. This combined with the buoyancy flux relation from (3.38) results in:

$$\theta_{v,0} - \theta_{v,ml} = \frac{C_{rad}z_i}{(A_{\theta_v} + 1)C_D|\vec{U}|}, \quad (6.3)$$

where C_{rad} is the radiative cooling in the case of a clear ABL.

$\theta_{v,ml}$ can be eliminated using (6.2) to yield

$$\begin{aligned} w_0(1 - e^{-z_i/z_w}) &= \frac{A_{\theta_v}C_{rad}z_i}{(A_{\theta_v} + 1)[(\theta_{ref} + \Gamma_{\theta}z_i)(1 + \epsilon_I q_{t,fa}) - \theta_{v,ml}]} \\ &= \frac{A_{\theta_v}C_D|\vec{U}|C_{rad}z_i}{C_D|\vec{U}|(A_{\theta_v} + 1)[(\theta_{ref} + \Gamma_{\theta}z_i)(1 + \epsilon_I q_{t,fa}) - \theta_{v,0}] + C_{rad}z_i} \end{aligned} \quad (6.4)$$

Now z_i is the only unknown and (6.4) can be rewritten as:

$$\begin{aligned} f(z_i) = z_i - \left\{ \frac{A_{\theta_v} + 1}{A_{\theta_v}C_{rad}} [(\theta_{ref} + \Gamma_{\theta}z_i)(1 + \epsilon_I q_{t,fa}) - \theta_{v,0}] \right. \\ \left. + \frac{z_i}{A_{\theta_v}C_D|\vec{U}|} \right\} w_0(1 - e^{-z_i/z_w}) = 0. \end{aligned} \quad (6.5)$$

This equation can then be numerically solved for z_i .

6.1.2 Case: cloudy ABL

For an initially cloudy ABL we need a different expression for the entrainment velocity, because now also radiative cooling from the cloud enhances entrainment. To get an idea of what effect a cloudy ABL has on the inversion height z_i the parametrization based on Moeng from (3.45) is being used.

In that equation we want to eliminate $\theta_{l,ml}$, therefore we use the steady-state equation for $\theta_{l,ml}$ from (3.56a).

Now we wish to obtain a similar expression as (6.5). As a first step, we rewrite (3.56a):

$$\frac{C_D|\vec{U}|}{C_D|\vec{U}| + w_e} [\Delta F_L - w_e(\theta_{ref} + \Gamma_{\theta}z_i - \theta_{l,0})] + w_e(\theta_{ref} + \Gamma_{\theta}z_i - \theta_{l,ml}) - \Delta F_L = 0. \quad (6.6)$$

By inserting (3.45) in (6.6) and using (3.56a) we get

$$\frac{C_D|\vec{U}|}{C_D|\vec{U}| + w_e} (A_{\theta_v} + 1) [\Delta F_L - w_e(\theta_{ref} + \Gamma_{\theta}z_i - \theta_{l,0})] + A_1 F' - \Delta F_L = 0. \quad (6.7)$$

This equation can be rewritten so that we get the following expression for w_e :

$$w_e = \frac{C_D |\vec{U}| (A_{\theta_v} \Delta F_L + A_1 F')}{(A_{\theta_v} + 1) C_D |\vec{U}| (\theta_{ref} + \Gamma_{\theta} z_i - \theta_{l,0}) + \Delta F_L - A_1 F'}. \quad (6.8)$$

We also know that in steady state $w_e = -\bar{w}$, from which it follows that

$$\frac{C_D |\vec{U}| (A_{\theta_v} \Delta F_L + A_1 F')}{(A_{\theta_v} + 1) C_D |\vec{U}| (\theta_{ref} + \Gamma_{\theta} z_i - \theta_{l,0}) + \Delta F_L - A_1 F'} = w_0 (1 - e^{-z_i/z_w}), \quad (6.9)$$

which can be rewritten to get an expression for $f(z_i) = 0$:

$$f(z_i) = z_i - \frac{1}{\Gamma_{\theta}} \left\{ \theta_{l,0} - \theta_{ref} + \frac{A_1 F' - \Delta F_L}{(A_{\theta_v} + 1) C_D |\vec{U}|} + \frac{(A_{\theta_v} \Delta F_L + A_1 F')}{(A_{\theta_v} + 1) w_0 (1 - e^{-z_i/z_w})} \right\} = 0. \quad (6.10)$$

This equation can be solved numerically for z_i . With the iterative method as described in section 3.2.5 we can determine the cloud base height, and using (3.47) we can calculate the *LWP*. If this *LWP* > 0 we have a cloudy ABL. If the *LWP* $= 0$ we have a clear ABL and then we use (6.5) to determine the steady-state solution of a clear ABL. A stable ABL is defined as the region where the *LWP* $= 0$ and $z_i < 0$. Physically this means that $w_e < -\bar{w}|_{z_i}$ at any time. The efficiency factor A_1 will be capped to $A_{1,max} = 1$, which means that A_1 does not increase further for *LWP* > 92 g/m². This is to prevent negative buoyancy fluxes which lead to decoupled solutions where the Mixed Layer Model is not valid anymore.

For plotting purposes we use the Low Tropospheric Stability (*LTS*) instead of θ_{ref} which is given by (5.9).

6.2 Numerical solutions

In this section the solutions of (6.5) and (6.10) will be presented for several experiments.

6.2.1 Experiment 1

The results for the first experiment with an initially clear and cloudy ABL are shown in Figure 6.1 and 6.2.

The initially clear ABL

What can be seen from Figure 6.1 is that there is a region where we have a stable ABL, that means: $z_i = 0$. We can see that this region appears around *LTS* ≥ 20 K. It means that in the stable region the entrainment is

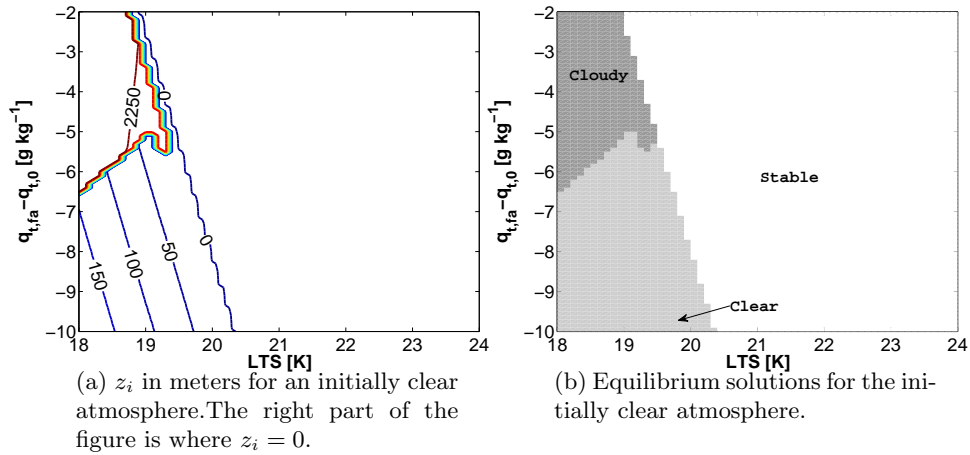


Figure 6.1: Experiment 1: steady state solutions for the variables z_i and the equilibrium states for the initially clear atmosphere.

not sufficient to counter the large scale subsidence and the inversion layer height decays to zero. We also have a region $18 \leq LTS < 20$ K where we keep a clear ABL. In this part the inversion height z_i remains below the diagnosed cloud base height z_b . When the free atmosphere becomes moister, the mixed layer total water content also increases, and that results in a lower cloud base. When the LTS decreases the inversion height z_i increases because it is easier then to entrain air from above the ABL into the mixed layer (which also follows from (3.39)). At the point where the inversion height is above the cloud base, we obtain a cloud and that enhances entrainment a lot resulting in a much deeper ABL and a very large LWP , as the cloud base does not increase as much as the inversion height.

The initially cloudy ABL

The results of the initially cloudy ABL are shown in Figure 6.2. What has been found is that the equilibrium state is, in contrast to the initially clear ABL, cloudy over the whole phase space. As can be seen from Figure 6.2a this also results in a much higher inversion height due to an enhanced entrainment by radiative cooling of the cloud, which is also responsible for the preservation of the cloud. Only in the region where the LTS is sufficiently high, we see a sharp decline in inversion height. From Figure 6.2b we can see that a moister free atmosphere results in a lower cloud base height z_b which is what we expect because according to (3.56b) a moister free atmosphere results in less drying of the mixed layer by entrainment. Consequently, a moister mixed layer becomes saturated at a lower height. In Figure 6.2c we can see that the LWP is, as a result of a deep ABL, very large (typically Stratocumulus clouds have a LWP of the order of 0.1 kg/m^2).

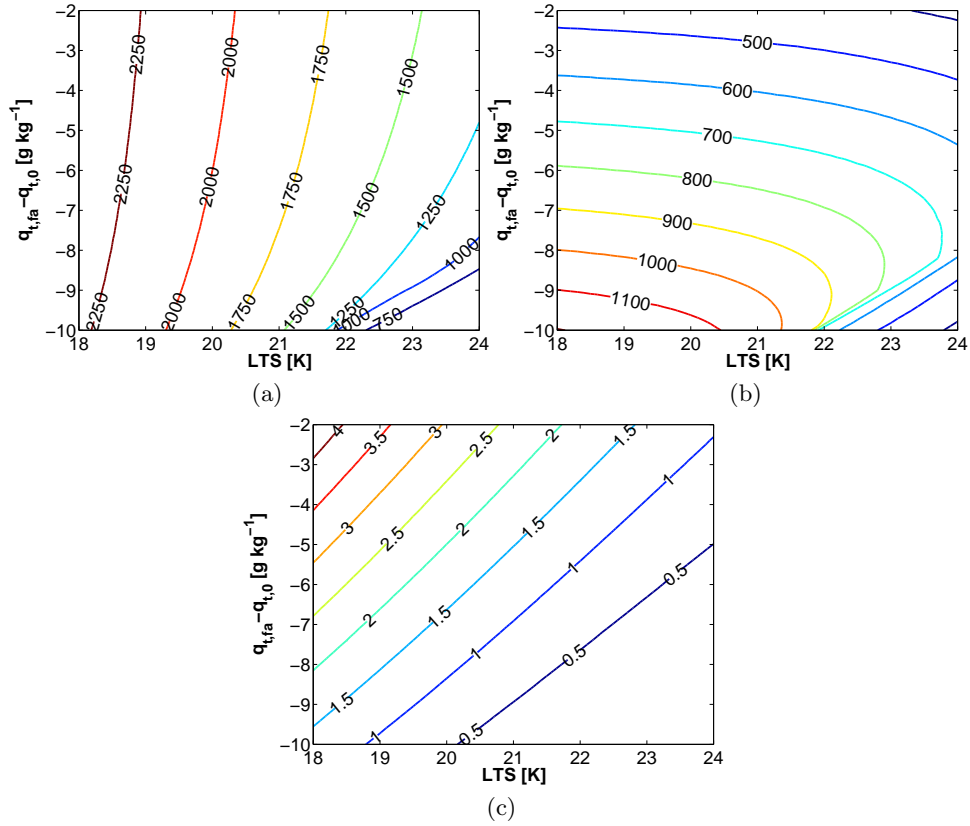


Figure 6.2: Experiment 1: steady state solutions for the initially cloudy atmosphere for a) z_i in meters, b) z_b in meters, and c) the LWP in kg/m^2 .

A thing we have to keep in mind is that the mixed layer model assumes that the ABL is vertically well mixed, which results in a lower cloud base height than in the case that there is a negative gradient in the total water content in the mixed layer, which could have on average over the ABL the same specific humidity, but has a much lower specific humidity at the top of the ABL than at the bottom of the ABL. This results in a thinner cloud because a decrease in the specific humidity at the top of the ABL results in a higher altitude where the air becomes saturated. The air at low altitude however does not become saturated, despite having a high specific humidity, due to the fact that the temperature is sufficiently high there.

And we have also not considered the process of decoupling in which the ABL separates into two layers.

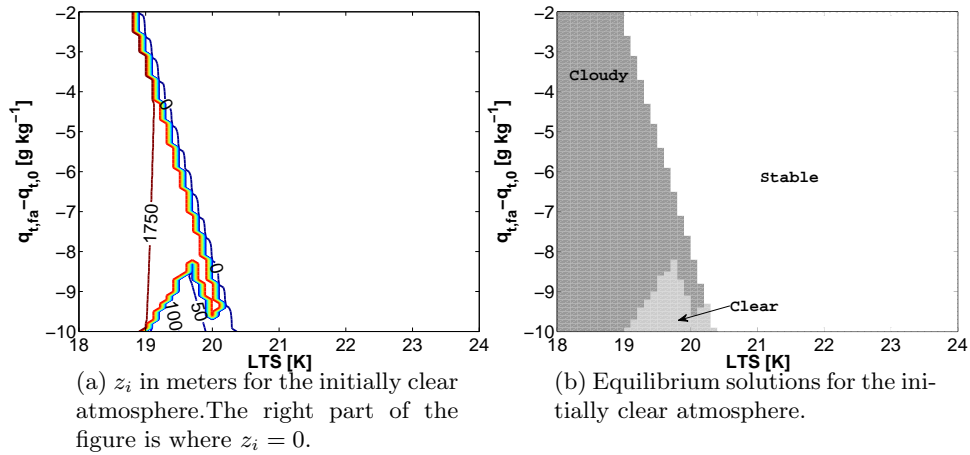


Figure 6.3: Experiment 2: steady state solutions for the variables z_i and the equilibrium states for the initially clear atmosphere.

6.2.2 Experiment 2

Experiment 2 is the same as experiment 1, except that we now use an increased wind speed.

The initially clear ABL

For the initially clear ABL we see the same case where the initial environmental conditions determine whether the final state is clear, cloudy or stable. The region where our final solution is $z_i = 0$ remains the same as in experiment 1. We do however see a smaller region where the final state is clear. From (3.56b) it follows that a higher wind speed results in a moister mixed layer. This in turn means that the air becomes saturated at a lower altitude. We thus have a larger region where $z_i > z_b$.

The initially cloudy ABL

For the initially cloudy ABL we can see that if we compare Figure 6.4a of experiment 2 with Figure 6.2a of experiment 1 that z_i has decreased. This can be explained with (6.10), which is depending on $|\vec{U}|$ and where an increase in $|\vec{U}|$ results in a lower z_i . If we compare Figure 6.4b with Figure 6.2b we can clearly see a decreased cloud base height. For the most part of the phase space the *LWP* has increased, except for the top left of the diagram.

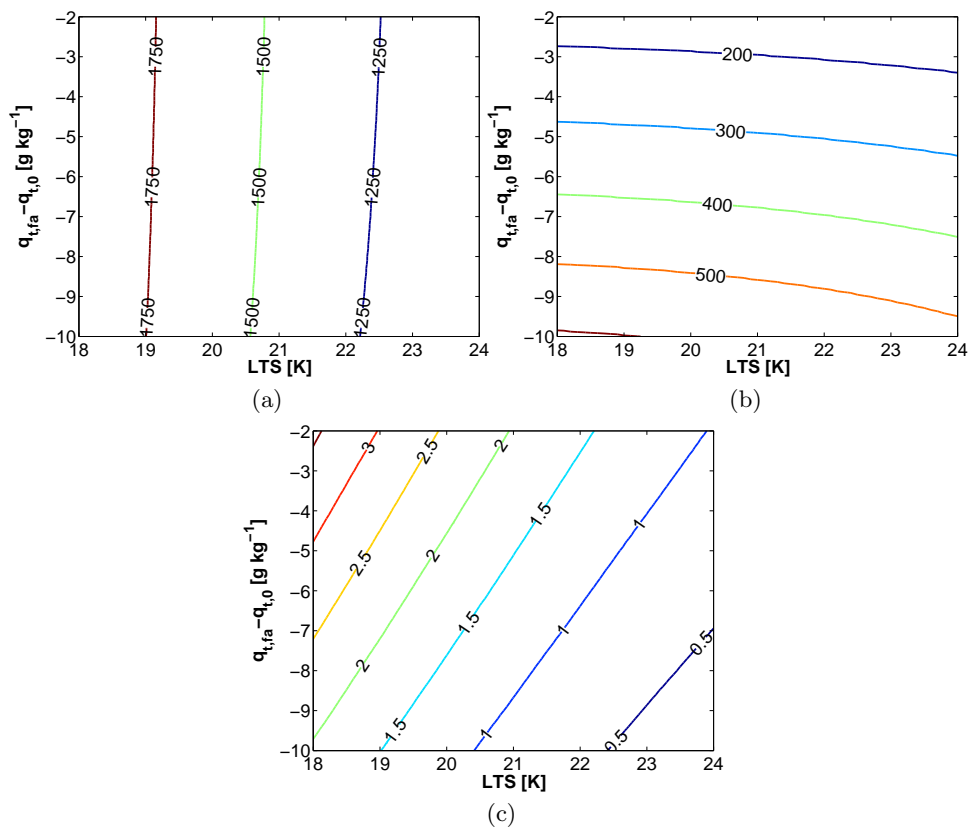


Figure 6.4: Experiment 2: steady state solutions for the initially cloudy atmosphere for a) z_i in meters, b) z_b in meters, and c) the LWP in kg/m^2 .

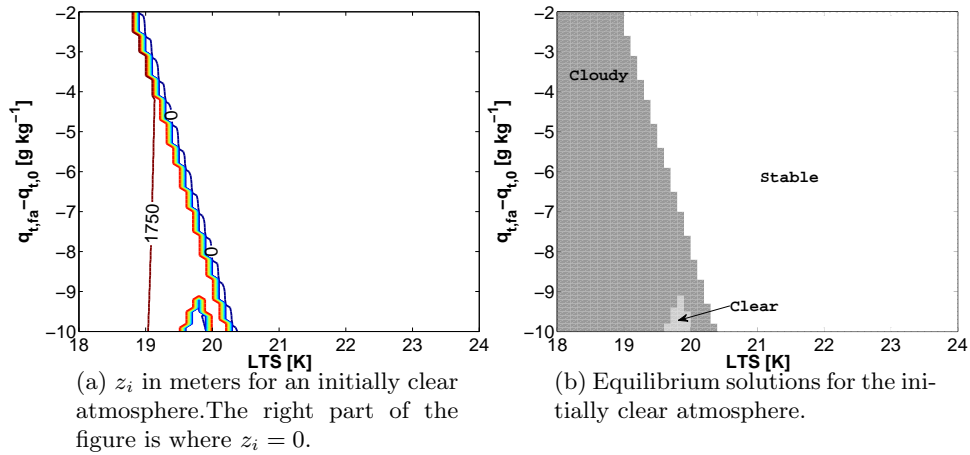


Figure 6.5: Experiment 3: steady state solutions for the variables z_i and the equilibrium states for the initially clear atmosphere.

6.2.3 Experiment 3

In experiment 3, we increase the SST with 2 K to 294 K, while we keep the same wind speed as in experiment 2.

For the initially clear ABL we can see in Figure 6.5b that in steady-state the region in the phase space where the atmosphere remains clear has greatly diminished.

In Figure 6.6 the steady-state solutions for the initially cloudy ABL are shown. If we compare Figure 6.6b with Figure 6.4b, we see a slight decrease in z_b . This has the consequence that in a larger area of the phase space $z_i > z_b$ and that the $LWP > 0$ which means that the ABL is cloudy. This explains the decreased 'clear' region in Figure 6.5b.

To make a more clear comparison between the experiments, Figure 6.7 has been included which shows the combined steady-state solutions of experiment 1 to 3 for the cross-section of $q_{t,fa} - q_{t,0} = -6$ g/kg. Figure 6.7a shows that all experiments with a wind speed of 6.74 m/s have a lower inversion height and that an increase in SST has no effect on the inversion height. This is a result of a constant LTS , where a shift in SST leads to the same shift of the temperature in the free atmosphere, which means that the size of the inversion jump at the cloud top stays the same.

From Figure 6.7b and Figure 6.7c it can also be seen that an increase in wind speed and SST lead to an increase of LWP .

If the conditions we have investigated are representative for a changing climate, and if the entrainment efficiency can be prescribed by (3.46), we see that a warmer climate has a negative feedback due to increased cloud thick-

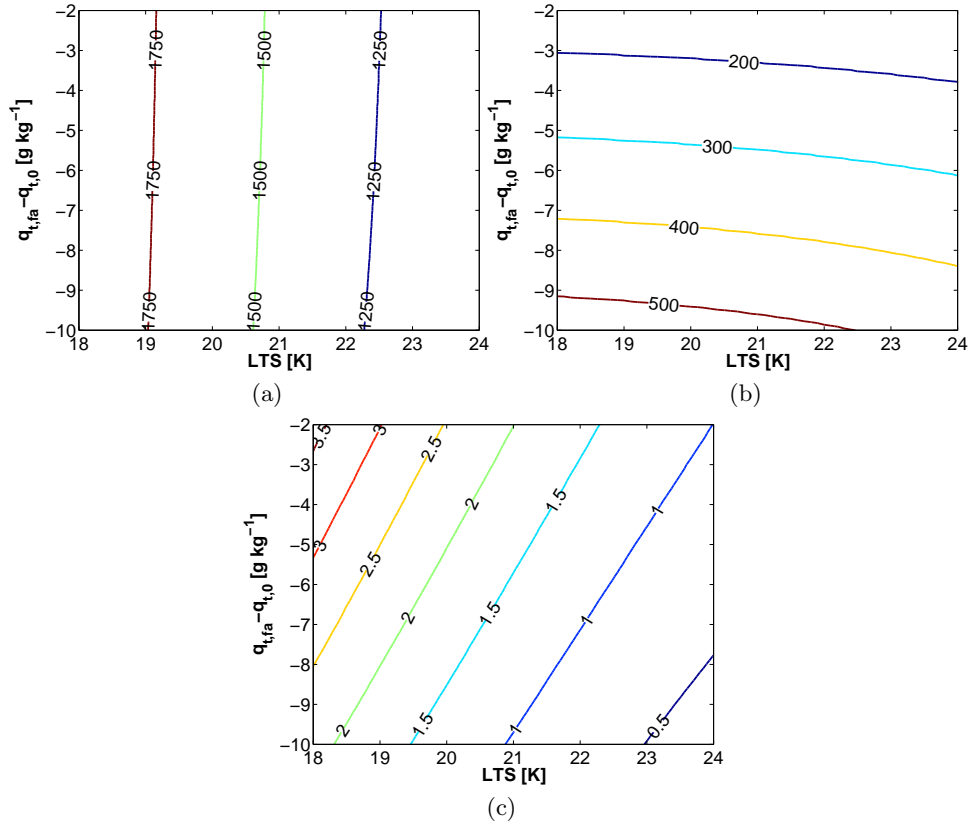


Figure 6.6: Experiment 3: steady state solutions for the initially cloudy atmosphere for a) z_i in meters, b) z_b in meters, and c) the LWP in kg/m².

ness.

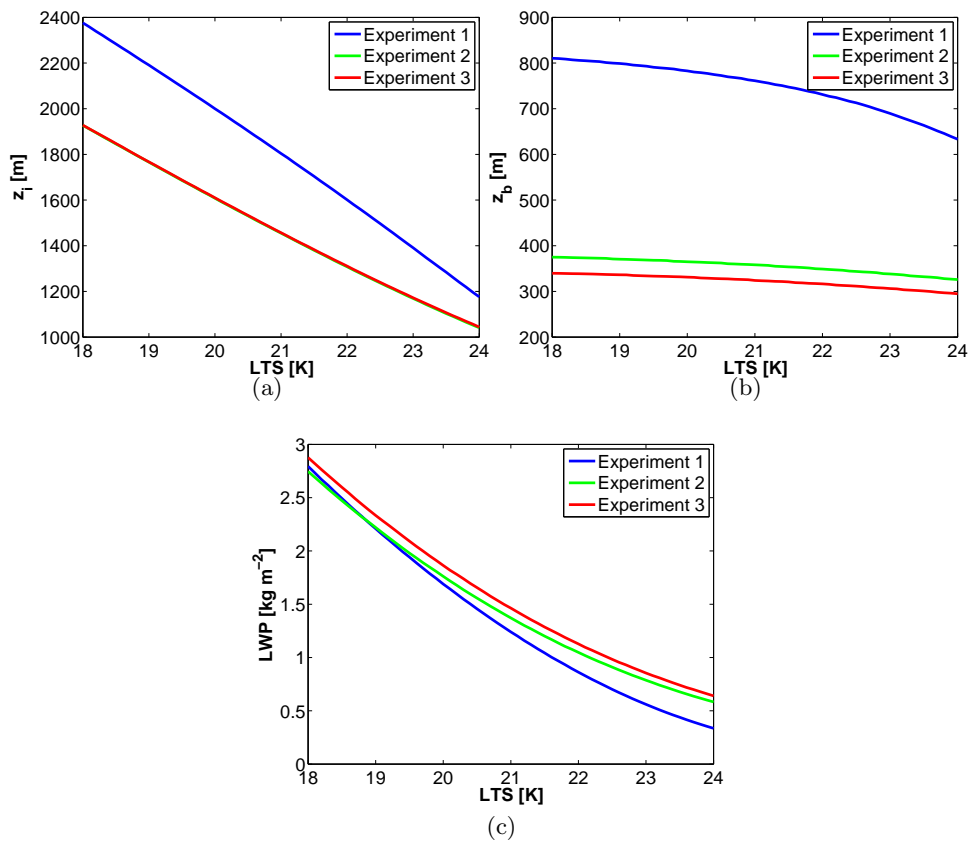


Figure 6.7: Combined steady-state solutions for the initially cloudy ABL for the cross-section of $q_{t,fa} - q_{t,0} = -6$ g/kg for a) z_i in meters, b) z_b in meters and c) the LWP in kg/m².

Chapter 7

A sensitivity study of Liquid Water Path for the STBL

The study of equilibrium states in chapter 6 will be elaborated on for the *LWP* in this chapter. Stratocumulus have a significant impact on the energy balance of the earth, because they are commonly found over the subtropical oceans and have a large area coverage and thus on average a high albedo. In a changing climate there is much uncertainty in the Sc cloud response, which is related to the *LWP* response. For instance, if the *LWP* increases, it would mean that a larger portion of the shortwave radiation reaching the ABL is reflected back into space comprising a negative feedback to global warming. This chapter will focus on small changes of four different parameters which have an effect on the *LWP*, to provide a better understanding of the effect of the different mechanisms that are involved in a changing climate.

7.1 Case setup

For simplicity, we will use a linear increasing subsidence instead of an exponential subsidence:

$$\bar{w} = -Dz, \quad (7.1)$$

where we choose for the divergence $D = 4 \cdot 10^{-6} \text{ s}^{-1}$.

We use again the most simple entrainment parametrization, that of Moeng: equation (3.45). It is assumed that in a STBL the radiative cooling dominates, that means $dF_L/\rho c_p \gg \overline{w'\theta'_l}|_0$. Therefore this parametrization can be simplified to:

$$w_e = \frac{AF'}{\Delta\theta_l}, \quad (7.2)$$

where $F' = \frac{dF_L}{\rho c_p}$ and A is the entrainment efficiency factor just as we saw in chapter 4, except that we take an arbitrary value for this efficiency factor and it is now also not depending on the *LWP* anymore.

We want to find an analytical expression for the steady-state inversion height z_i , which can be found as follows: Firstly we have from (7.2):

$$w_e = \frac{AF'}{\Delta\theta_l} = \frac{AF'}{\theta_{ref} + \Gamma_\theta z_i - \theta_{l,ml}} \quad (7.3)$$

$$= \frac{AF'}{LTS + \Gamma_\theta(z_i - z_{LTS}) + \theta_{l,0} - \theta_{l,ml}}.$$

For $\theta_{l,ml}$ we have the steady-state equation which is based on (3.56a) and reads

$$\theta_{l,ml} = \theta_{l,0} + \frac{Dz_i[LTS + \Gamma_\theta(z_i - z_{LTS})] - F'}{C_D|\vec{U}| + Dz_i}, \quad (7.4)$$

where we have replaced ΔF_L by F' where we assume that $1 - e^{-\kappa \cdot LWP} \approx 1$, and θ_{ref} has been replaced by the LTS . (7.4) can be inserted into (7.3) and combined with (3.58) this can be solved for z_i :

$$z_i = -\frac{Q_1}{2\Gamma_\theta} + \frac{1}{2\Gamma_\theta} \sqrt{Q_1^2 + \frac{4AF'\Gamma_\theta}{D}}, \quad (7.5)$$

with $Q_1 = LTS - \Gamma_\theta z_{LTS} + \frac{(1-A)F'}{C_D|\vec{U}|}$. Based on (3.56b) we have for $q_{t,ml}$ the following equation :

$$q_{t,ml} = q_{t,0} + \frac{Dz_i(q_{t,fa} - q_{t,0})}{C_D|\vec{U}| + Dz_i}. \quad (7.6)$$

Now the cloud base height z_b can be calculated following the procedure of section 3.2.5. The LWP can then be calculated using (3.47).

If we now consider a small change of the LWP as a function of the free parameters, then ΔLWP can be approximated by

$$\Delta LWP \approx \sum_{i=1}^N dx_i \left(\frac{\partial LWP}{\partial x_i} \right). \quad (7.7)$$

For each free parameter, we will estimate the partial derivative by using finite differences, which means

$$\left(\frac{\partial LWP}{\partial x_i} \right)_{x_1, \dots, x_{i-1}, \dots, x_{i+1}, \dots, x_N} \approx \frac{dLWP}{dx_i}. \quad (7.8)$$

The free parameters upon which the partial derivatives are based are the entrainment efficiency A , the SST , D and $|\vec{U}|$. For $\frac{\partial LWP}{\partial SST}$ it means that as a consequence of a small increase in SST , $\theta_{l,0}$ and $q_{t,0}$ will also increase slightly. We keep however $(q_{t,fa} - q_{t,0})$ constant, so that means that $q_{t,fa}$ will increase the same amount as $q_{t,0}$ does. A summary of the parameters used can be seen in Table 7.1.

Parameter	Value
Γ_θ (K/m)	$6 \cdot 10^{-3}$
C_D	0.001
ρ_0 (kg/m ³)	1.14
dF_L (W/m ²)	35
F' (K m/s)	0.031
p_s (hPa)	1020
A	1
D (s ⁻¹)	$4 \cdot 10^{-6}$
$ \vec{U} $ (m/s)	8
SST (K)	290
LTS (K)	[18, 24]
$q_{t,fa} - q_{t,0}$ (kgkg ⁻¹)	[-0.010, -0.002]

Table 7.1: The values of the parameters used for Figure 7.1.

7.2 Numerical results

The results of the LWP and the derivatives of the LWP can be viewed in Figure 7.1. What can be seen for the first derivative, that is $\frac{\partial LWP}{\partial A}$ in Figure 7.1b, that there is an area in the left hand part of the figure where an increase in A leads to an increase of the LWP . But we can also see in the right-bottom part of the figure a region where the LWP decreases when the entrainment efficiency increases. $z_i \sim \frac{w_e}{D}$ but we also know that z_b increases when w_e increases. It can be concluded that for the region where $\frac{\partial LWP}{\partial A} > 0$, $\Delta z_i > \Delta z_b$ and for the region where $\frac{\partial LWP}{\partial A} < 0$ it is the opposite.

From Figure 7.1e we can see that in the case that q_{FA} shifts the same amount as $q_{t,0}$, an increase of SST leads to an increase of LWP , independent of the environmental conditions. This is in agreement with what we found in chapter 6. However, if we would keep a constant q_{FA} things change drastically, as shown in Figure 7.1f, where now an increase in SST leads to a decrease of LWP . This can be explained by considering that a non shifting free atmosphere and an increase in SST lead to a moister and warmer mixed layer, but the inversion jump of specific humidity also increases which leads to more drying than in the case that the inversion jump of specific humidity stays constant, as in Figure 7.1e.

Figure 7.1c shows that an increase in divergence leads to a decrease of LWP . This is a result of an increased subsidence which pushes down the ABL leading to a thinner cloud.

As shown in Figure 7.1d, an increased wind speed results in a larger LWP , which is in agreement with the results from chapter 6. This is because an increase in wind speed corresponds with increased surface fluxes, which leads

to a larger total water content q_t in the mixed layer.

Figure 7.1 shows that the partial derivatives each have a contribution to an increase of that variable. In a changing climate, the outcome of the sum of contributions of the partial derivatives depends on what parameters are actually sensitive to a warmer climate. Suppose that a warmer climate leads to a higher entrainment efficiency, because a higher temperature is correlated with more turbulent kinetic energy, leading to more entrainment. If $dA = 0.1$, the change in LWP would be 10% of the values shown in Figure 7.1b, which makes this contribution much less than it appears at first sight.

According to the CGILS framework (CGILS, 2008), we expect in a warmer climate a weakening of the Hadley circulation, which leads to a smaller divergence. This would imply an increase in LWP .

If the specific humidity of the free atmosphere shifts the same amount as the specific humidity at the sea surface, there would be an increase of cloud thickness which is a negative climate feedback.

If the specific humidity of the free atmosphere does not shift the climate feedback is positive.

However, the cloud response appears to be the most sensitive to a change in divergence, which appears to be a negative feedback as the divergence will decrease. Therefore in general there tends to be a negative feedback to a changing climate based on the sum of these derivatives.

This is not in agreement with the results from GALES in chapter 5 where we found a positive feedback. An explanation for this discrepancy in steady-state results is that the MLM does not incorporate possible decoupling effects where the ABL is vertically not well-mixed and moist thermals cannot reach the cloud layer. The result of that is that the actual cloud base height can be much higher than the MLM predicts. We have seen in chapter 5 that this decoupling can even lead to the dissipation of the cloud.

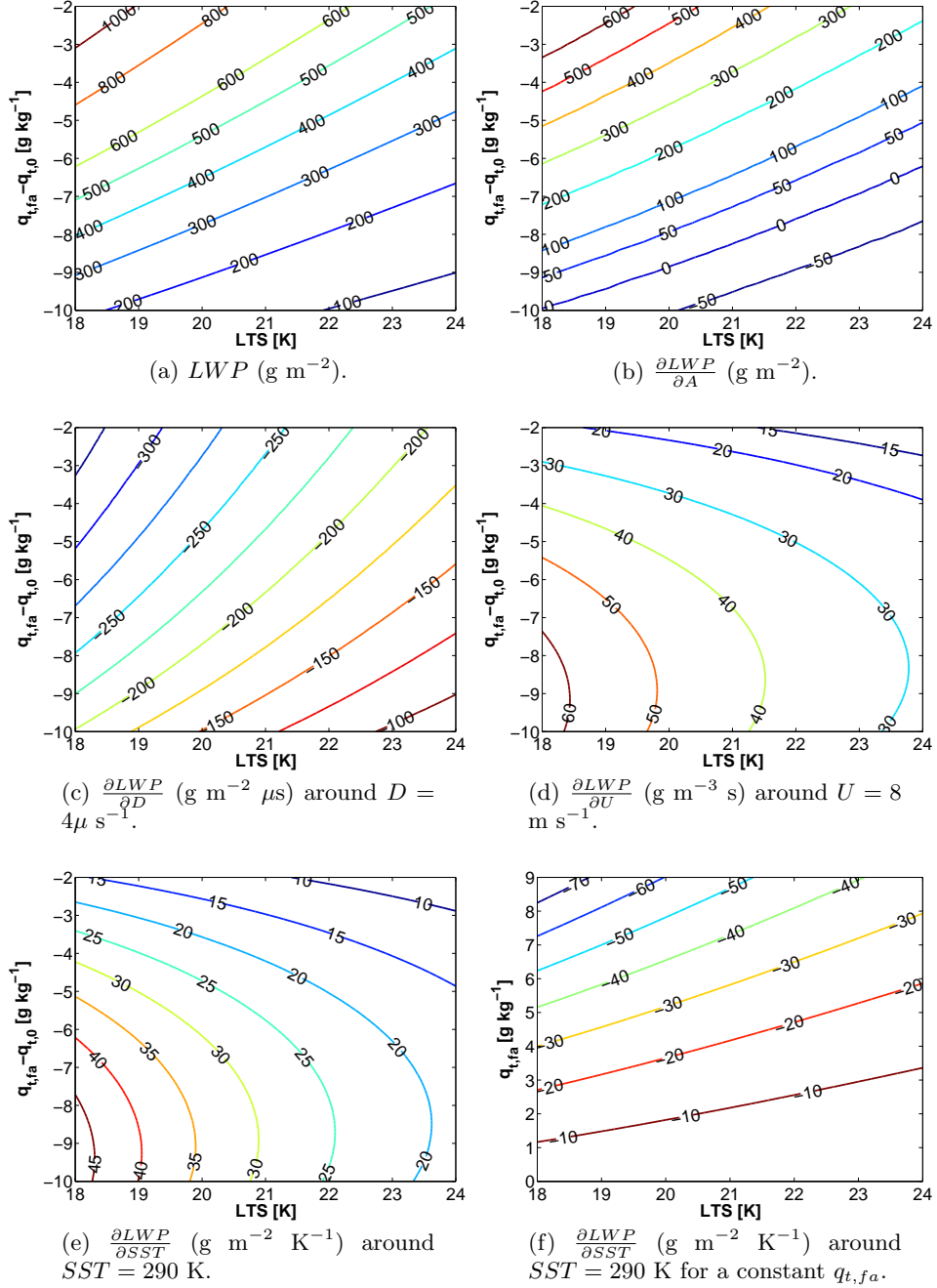


Figure 7.1: The partial derivatives of the LWP .

Chapter 8

Conclusions and recommendations

8.1 Conclusions

8.1.1 CGILS: GALES steady-state analysis

In the study of the phase space consisting of LTS and specific humidity using an exponential subsidence following Bellon and Stevens (2012) we have found steady-state solutions. We have found in a +2 K SST scenario a thinning of the Sc. This thinning was the highest in regions with a very high stable stratification corresponding to a high LTS . This is a clear **positive feedback**. For lower LTS we see a slight decrease in LWP except for $LTS = 17.7$ K where we see a slight increase in LWP . For the case where we decrease the inversion jump of specific humidity by 2 g/kg we have seen a slight decrease of LWP in a changing climate.

We have seen that if the LTS reaches a value of $LTS = 15.7$ K and $q_{FA} = 5.2$ g/kg or $LTS = 17.7$ K and $q_{FA} = 3.2$ g/kg that the Sc cloud becomes thermodynamically unstable, dissolves and a clear atmosphere remains. We have obtained a similar result for the perturbed climate.

In general we can conclude that in a changing climate we obtain a **positive Sc cloud feedback**.

The conclusion of the comparison between GALES and SCM results with the same initial conditions and forcings is that they are in general not in agreement.

8.1.2 EUROCS

To study equilibrium states in CGILS, we needed a constant diurnally averaged radiative forcing. By simulating the EUROCS case with GALES we have assessed the use of a constant radiation which is the same as the mean of the diurnal cycle. We have found a moderate decrease of the LWP

by 10% in the case that we use a constant diurnally averaged radiation instead of a diurnal cycle of the radiation. This justified the use of a constant diurnally averaged radiation in CGILS.

8.1.3 Equilibrium states with the Mixed-Layer Model

In chapter 6 we have investigated equilibrium states of Sc using the MLM. By using an exponential subsidence following Bellon and Stevens (2012) and using the entrainment parametrization of Moeng (2000), we have seen that given an initially clear boundary layer, we have a region in the phase space which remains clear, a region which goes to a stable clear state and a region which turns cloudy on long times. If we start with an initially cloudy boundary layer it remains cloudy as a result of increased entrainment due to enhanced radiative cooling. This result differs from the CGILS results where we have seen that an initially cloudy ABL could under certain conditions (low LTS , low q_{FA}) transition to a clear ABL. We have seen that an increased wind speed and increased SST both lead for an initially clear boundary layer to a smaller region which remains clear for long times. An increased wind speed and SST also lead to a slight thickening of the Sc.

8.1.4 Sensitivity analysis of LWP with the Mixed-Layer Model

In the sensitivity analysis of LWP we have used a simplified version of the entrainment parametrization of Moeng (2000). We have studied the influence on LWP of a small change of entrainment efficiency, divergence, wind speed, and SST for both a changing FA and a constant FA. An increase in entrainment efficiency results for the most part of the phase space in an increase of LWP , but for large LTS and large specific humidity jump there is actually a decrease of LWP .

In a changing climate we expect a lower divergence. We have seen that a smaller divergence gives a much larger LWP .

An increase of wind speed also results in a thickening of the Sc which is correlated with increased surface fluxes leading to a lower cloud base. If the free atmosphere does not shift the same amount as the specific humidity at the sea surface, we see a thinning of the Sc in a +2 K SST scenario. If however the specific humidity in the FA shifts the same amount as the specific humidity at the sea surface we see a thickening of the Sc. This is not in agreement with the GALES results for a changing climate where the specific humidity in the FA shifts the same amount as the specific humidity at the sea surface.

The discrepancy in cloud response between GALES and the MLM can be explained by the effect of decoupling which the MLM cannot handle. This makes GALES more realistic. Decoupling has the consequence that the

cloud base level is much higher than the value predicted by the MLM, which is why the MLM should be used carefully.

8.2 Recommendations

8.2.1 A diurnal cycle of the solar radiation

We have seen that the *LWP* and entrainment follow a diurnal cycle when we use a diurnal radiative forcing instead of a constant diurnally averaged radiative forcing. By using a constant diurnally averaged radiative forcing, it is possible to obtain a steady-state. Despite of the small difference, one should keep in mind that a constant diurnally averaged radiative forcing results, diurnally averaged, in a lower *LWP*.

8.2.2 CGILS

We used GALES to investigate the framework provided by the CGILS project. It would be interesting to extent the investigation of the phase space consisting of the inversion jumps of temperature and specific humidity to a larger set of atmospheric conditions. This could provide additional insight in the cloud feedback response of a changing climate for a wide variety of atmospheric conditions. Considering a Stratocumulus-Topped Boundary Layer, it is interesting to find a criterion which separates Sc steady-states from Shallow Cumulus steady-states.

We have seen that there is disagreement between the GALES results and the SCM Ec-Earth results. Further evaluation of these models with field results should be done to validate and improve those models.

8.2.3 Mixed-Layer Model sensitivity study

The Mixed-Layer Model has been very useful to provide insight in the dynamics of Sc. The sensitivity of the thickness of the cloud as a function of several parameters can provide much information of the effect of these parameters. An important next step is to quantify the changes of these parameters (ie. wind speed, subsidence, entrainment efficiency) in a changing climate. In this way the determination of the Sc cloud response can be more accurate.

A feature that has not been used is precipitation. This has some thermodynamic effects, including the effect that it could lower the amount of liquid water droplets in a cloud, which could cause a thinning of the cloud.

Finally horizontal advection could be implemented to incorporate more realistic boundary conditions.

Acknowledgements

I want to thank Stephan de Roode for his inspiring lectures, support and feedback.

Jerome Schalkwijk for the development and support of GALES.

Sara Dal Gesso for discussing the experimental set up and providing SCM Ec-Earth results.

Johan van der Dussen for giving support on the experimental set up and physics of Sc.

Steeff Böing for his Linux support.

And I want to thank Erwin de Beus for all his IT support to make sure the network, the computer and GALES works.

Bibliography

Bellon, G. and B. Stevens, *Using the sensitivity of large-eddy simulations to evaluate atmospheric-boundary layer*. Journal of the Atmospheric Sciences, 2012.

E. Boeker and R. van Grondelle, *Environmental Physics Second Edition*. John Wiley & Sons, Ltd, 1999.

CGILS (2008): http://atmgcm.msrc.sunysb.edu/cfmip_figs/Case_specification.html

J.A.Curry and E.E. Ebert, *Annual Cycle of Radiation Fluxes over the Arctic Ocean: Sensitivity to Cloud Optical Properties*, American Meteorological Society, 1992.

J.W. Deardorff, *Stratocumulus-capped mixed layers derived from a three dimensional model*, Boundary Layer Meteorology, 18: 495-527, 1980.

J.W. Deardorff, *Cloud Top Entrainment Instability*, American Meteorological Society, 1980.

S.R. de Roode, *Clouds*. University of Utrecht, 2004.

J. Dufresne and S. Bony, *An Assessment of the Primary Sources of Spread of Global Warming Estimates from Coupled Atmosphere-Ocean Models*. American Meteorological Society, 2008.

P. G. Duynkerke et al, *Observations and numerical simulations of the diurnal cycle of the EUROCS stratocumulus case*. Quarterly Journal of the Royal Meteorological Society, 130: 3269-3296, 2004.

T. Heus et al, *Formulation of the Dutch Atmospheric Large-Eddy Simulation (DALES) and overview of its applications*. Geoscientific Model Development, 3: 415-444, 2010.

The International Satellite Cloud Climatology Project (ISCCP), <http://isccp.giss.nasa.gov/>.

C.H. Moeng, *Entrainment rate, cloud fraction and liquid water path of planetary boundary layer stratocumulus clouds*. Journal of the Atmospheric Sciences, 57:3627-3643, 2000.

- S.B. Pope, *Turbulent Flows*, 2000.
- D.A. Randall, *Conditional Instability of the First Kind Upside-Down*, American Meteorological Society, 1980.
- V. Savic-Jovicic and B. Stevens, *The Structure and Mesoscale Organization of Precipitating Stratocumulus*. *Journal of the Atmospheric Sciences*, 65:1587-1605, 2007.
- B. Stevens, *Bulk boundary-layer concepts for simplified models of tropical dynamics*. *Theoretical and Computational Fluid Dynamics*, 20: 279-304, 2006.
- R.B. Stull, *An Introduction to Boundary Layer Meteorology*, 1986.
- R. van Driel, *Response of a Dry Convective Boundary Layer to Non-Stationary Surface Heat Fluxes*. Master's thesis, Delft University of Technology, 2010.
- J.M. van Wessem, *Mixed-Layer Model Solutions of Equilibrium States of Stratocumulus-Topped Boundary Layers*. Master's thesis, Delft University of Technology, 2011.
- John M. Wallace and Peter V. Hobbs, *Atmospheric Science: An Introductory Survey*. University of Washington, 2006.
- G. Woan, *The Cambridge Handbook of Physics Formulas*. Cambridge University Press, 2003.
- Robert Wood and Christopher S. Bretherton, *Boundary Layer Depth, Entrainment, and Decoupling in the Cloud-Capped Subtropical and Tropical Marine Boundary Layer*. *Journal of Climate*, 35:3576-3588, 2004.

Appendix A

Namoptions GALEs for the EUROCS case

```
&RUN
iexpnr = 001
lwarmstart = .false.
runtime = 864000.
startfile = 'initd144h00m.028'
trestart = 14400.
dtmax = 10.
ladaptive = .true.
irandom = 43
randthl = 0.1
randqt = 0.
nsv = 0
```

```
&DOMAIN
imax = 128
jtot = 128
kmax = 121
xsize = 6400.
ysize = 6400.
xlat = 33.3
xlon = -119.5
xday = 197
xtime = 8.
ksp = 106
```

```
&NAMMICROPHYSICS
imicro = 0
```

&DEBUG

ldebug = .false.

&PHYSICS

z0 = 2e-4

ustin = 0.18

ps = 101250.00

thls = 288.0

wtsurf = 0.01211

wqsurf = 3.82e-5

lmoist = .true.

isurf = 2

timerad = 0.

lcoriol = .true.

ltimedep = .false.

iradiation = 2

rad_ls = .true.

rad_longw = .true.

rad_shortw = .true.

rad_smoke = .false.

dlwbot = 0

dlwtop = 70

&DYNAMICS

llsadv = .false.

lqlnr = .false.

cu = 3.44146

cv = -4.91491

iadv_mom = 5

iadv_tke = 55

iadv_thl = 55

iadv_qt = 55

iadv_sv = 55

&NAMCHECKSIM

tcheck = 60

&NAMSAMPLING

lsampcl = .false.

dtav = 60

timeav = 600

&NAMTIMESTAT

ltimestat = .true.

dtav = 60

&NAMCROSSSECTION

lcross = .false.

dtav = 60

&NAMGENSTAT

lstat = .true.

dtav = 60

timeav = 600

&NAMFIELDDDUMP

lfielddump = .false.

dtav = 10

ldiracc = .true.

&NAMSTATTEND

dtav = 60

timeav = 600

ltend = .true.

&SUBGRID

ldelta = .false.

cm = 0.12

cn = 0.76

ch1 = 1.

ch2 = 2.

ce1 = 0.19

ce2 = 0.51

&NAMTILT

ltilted = .false.

alfa = 0.0

dtav = 1.

timeav = 10.

lstat = .true.

&NAMBUDGET

lbudget = .true.

dtav = 60.

timeav = 600.

&NAM_SCALAR_BUDGETS

lbudg_thlvar = .false.
dtav = 1
timeav = 5

&NAMFIELDDDUMP

lfielddump = .false.
dtav = 600
ldiracc = .false.

&NAMPARTICLES

lpartic = .false.
dtpart = 6.
intmeth = 3
dtav = 60.
timeav = 600.
timedump = 6
npartdump = 10
lpartsgs = .true.

&NAMSAMPLING

lsampcl = .false.
dtav = 60
timeav = 600

&NAMRADSTAT

dtav = 60
timeav = 600.
lstat = .true.

Appendix B

CGILS: namoptions GALES for the control case

```
&RUN
iexpnr = 019
lwarmstart = .false.
runtime = 2592000.
startfile = 'initd240h00m.039'
trestart = 43200.
dtmax = 15.
ladaptive = .true.
irandom = 43
randthl = 0.1
randqt = 0.
nsv = 0
```

```
&DOMAIN
imax = 128
jtot = 128
kmax = 161
xsize = 6400.
ysize = 6400.
xlat = 32.
xlon = 129.
xday = 195
xtime = 15.
ksp = 146
```

```
&NAMMICROPHYSICS
```

imicro = 0

&DEBUG

ldebug = .false.

&PHYSICS

z0 = 2e-4

ustin = 0.18

ps = 101280.00

thls = 290.9401

wtsurf = 0.01211

wqsurf = 3.82e-5

lmoist = .true.

isurf = 2

timerad = 0.

lcoriol = .true.

ltimedep = .false.

iradiation = 2

rad_ls = .true.

rad_longw = .true.

rad_shortw = .true.

rad_smoke = .false.

sfc_albedo = 0.07

sw0 = 405.

dlwtop = 70.

dlwbot = 13.3

&DYNAMICS

llsadv = .false.

lqlnr = .false.

cu = 0.

cv = -6.74

iadv_mom = 5

iadv_tke = 55

iadv_thl = 55

iadv_qt = 55

iadv_sv = 55

lambda_crit = 20

&NAMCHECKSIM

tcheck = 60

&NAMSAMPLING

lsampcl = .false.

dtav = 60

timeav = 600

&NAMTIMESTAT

ltimestat = .true.

dtav = 60

iblh_meth = 2

&NAMCROSSSECTION

lcross = .false.

dtav = 60

&NAMGENSTAT

lstat = .true.

dtav = 60

timeav = 600

&NAMFIELDDUMP

lfielddump = .false.

dtav = 10

ldiracc = .true.

&NAMSTATTEND

dtav = 60

timeav = 600

ltend = .true.

&SUBGRID

ldelta = .false.

cm = 0.12

cn = 0.76

ch1 = 1.
ch2 = 2.
ce1 = 0.19
ce2 = 0.51

&NAMTILT
ltilted = .false.
alfa = 0.0
dtav = 1.
timeav = 10.
lstat = .true.

&NAMBUDGET
lbudget = .true.
dtav = 60.
timeav = 600.

&NAM_SCALAR_BUDGETS
lbudg_thlvar = .false.
dtav = 1
timeav = 5

&NAMFIELDDUMP
lfielddump = .false.
dtav = 600
ldiracc = .false.

&NAMPARTICLES
lpartic = .false.
dtpart = 6.
intmeth = 3
dtav = 60.
timeav = 600.
timedump = 6
npartdump = 10
lpartsgs = .true.

&NAMSAMPLING

```
lsampcl = .false.  
dtav = 60  
timeav = 600
```

```
&NAMRADSTAT  
dtav = 60  
timeav = 600.  
lstat = .true.
```